





# Fullerenol C<sub>60</sub>(OH)<sub>40</sub> Nanoparticles and Ectoine Protect Human Nasal Epithelial Cells Against the Cytokine Storm After Addition of the Full-Length Spike Protein from SARS-CoV-2

Malwina Sosnowska <sup>1</sup>, Mateusz Wierzbicki <sup>1</sup>, Barbara Nasiłowska <sup>2</sup>, Totka Nikolaeva Bakalova<sup>3</sup>, Klara Piotrowska<sup>4</sup>, Barbara Strojny-Cieślak <sup>1</sup>, Ewa Sawosz<sup>1</sup>, Marta Kutwin<sup>1</sup>

<sup>1</sup>Department of Nanobiotechnology, Institute of Biology, Warsaw University of Life Sciences, Warsaw, Poland; <sup>2</sup>Biomedical Engineering Center, Institute of Optoelectronics, Military University of Technology, Warsaw, Poland; <sup>3</sup>Department of Material Science, Faculty of Mechanical Engineering, Technical University of Liberec, Liberec, Czech Republic; <sup>4</sup>Department of Animal Nutrition, Institute of Animal Sciences, Warsaw University of Life Sciences, Warsaw, Poland

Correspondence: Malwina Sosnowska, Department of Nanobiotechnology, Institute of Biology, Warsaw University of Life Sciences, st. Ciszewskiego 8, Warsaw, 02-786, Poland, Tel +48 22 593 66 71, Email malwina\_sosnowska@sggw.edu.pl

**Introduction and Objective:** Severe acute respiratory syndrome coronavirus 2 (SARS-CoV-2) enters the nasal cavity, penetrates the nasal epithelial cells through the interaction of its spike protein with the host cell receptor angiotensin-converting enzyme 2 (ACE2) and then triggers a cytokine storm. We aimed to assess the biocompatibility of fullerenol nanoparticles C<sub>60</sub>(OH)<sub>40</sub> and ectoine, and to document their effect on the protection of primary human nasal epithelial cells (HNEpCs) against the effects of interaction with the fragment of virus - spike protein. This preliminary research is the first step towards the construction of an intranasal medical device with a protective, mechanical function against SARS-CoV-2 similar to that of personal protective equipment (eg masks).

**Methods:** We used HNEpCs and the full-length spike protein from SARS-CoV-2 to mimic the first stage of virus infection. We assessed cell viability with the XTT assay and a spectrophotometer. May-Grünwald Giemsa and periodic acid-Schiff staining served to evaluate HNEpC morphology. We assessed reactive oxygen species (ROS) production by using 2',7'-dichlorofluorescein diacetate and commercial kit. Finally, we employed reverse transcription polymerase chain reaction, Western blotting and confocal microscopy to determine the expression of angiotensin-converting enzyme 2 (ACE2) and inflammatory cytokines.

**Results:** There was normal morphology and unchanged viability of HNEpCs after incubation with 10 mg/L C<sub>60</sub>(OH)<sub>40</sub>, 0.2% ectoine or their composite for 24 h. The spike protein exerted cytotoxicity via ROS production. Preincubation with the composite protected HNEpCs against the interaction between the spike protein and the host membrane and prevented the production of key cytokines characteristic of severe coronavirus disease 2019, including interleukin 6 and 8, monocyte chemotactic protein 1 and 2, tissue inhibitor of metalloproteinases 2 and macrophage colony-stimulating factor.

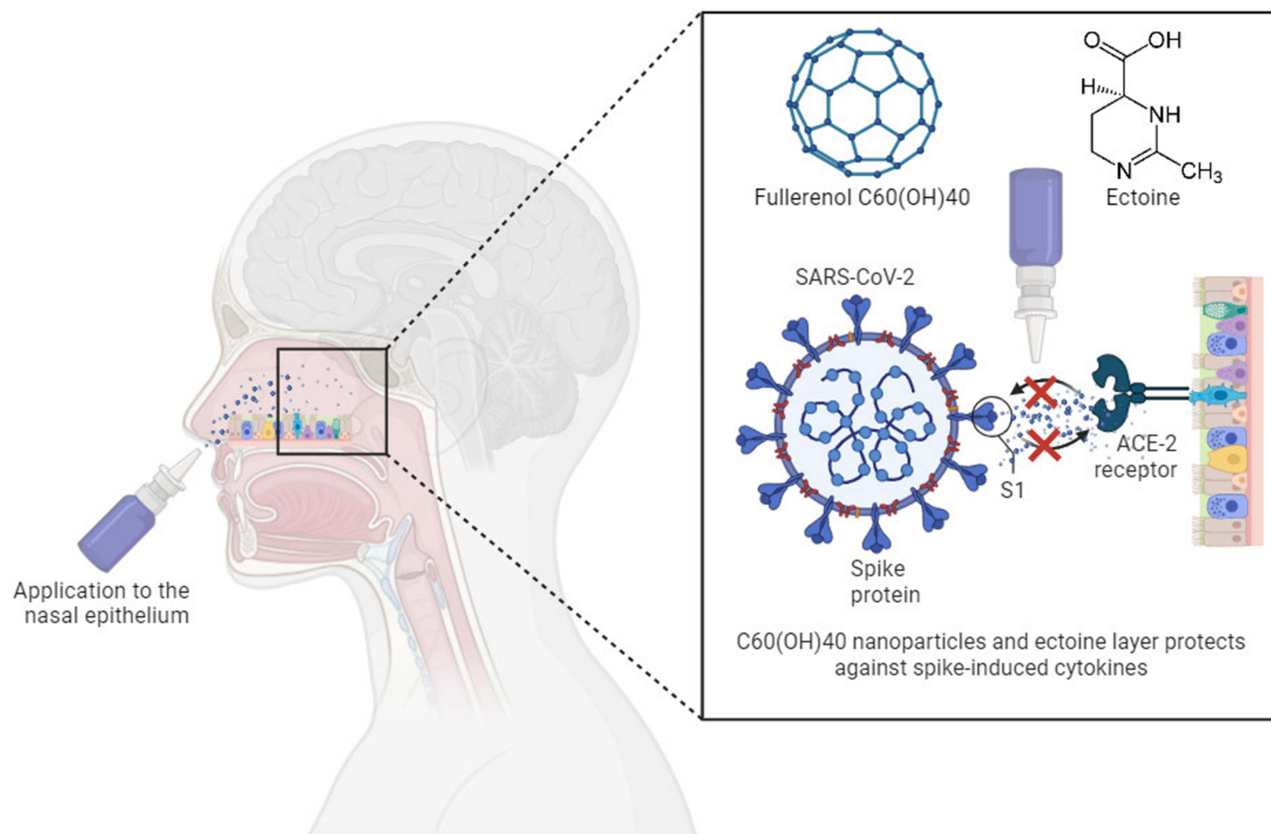
**Conclusion:** In the future, the combination of fullerenol and ectoine may be used to prevent viral infections as an intranasal medical device for people with reduced immunity and damaged mucous membrane.

**Keywords:** ACE2, cytokine storm, ectoine, nasal epithelium, polyhydroxylated fullerene, spike

## Introduction

Severe acute respiratory syndrome coronavirus 2 (SARS-CoV-2) first appeared in December 2019 in Wuhan, China. This virus causes the disease known as coronavirus disease 2019 (COVID-19). The high infectiousness of SARS-CoV-2 led to its rapid spread throughout the world in a very short time and the global coronavirus disease 2019 (COVID-19) pandemic. Since the beginning of the epidemic, 703 million SARS-CoV-2 infections have been recorded worldwide, including 6.9 million deaths.<sup>1</sup>

Graphical Abstract



SARS-CoV-2 is a betacoronavirus with a size of 120–160 nm. It comprises four structural proteins: spike (S), envelope (M), membrane (E) and nucleocapsid (N). The N protein is directly associated with viral RNA and is responsible for viral replication and the host cell’s cellular response during infection. The remaining structural proteins – S, E and M – are located outside the viral RNA. SARS-CoV-2 is a positive-sense single-stranded RNA (+ssRNA) virus. Its genome is 30 kilobases (kb) and encodes 29 proteins from 15 open reading frames. Mutations in the S protein, particularly in its receptor-binding domain (RBD), have resulted in the rapid emergence of numerous variants, including Alpha, Beta, Gamma, Delta, Omicron and Kraken. The RBD is responsible for the interaction between the virus and host cells. It is mutated constantly, so it is difficult to acquire collective immunity.<sup>1</sup> However, the S protein or only its RBD is highly immunogenic, and is has been used in subunit vaccines to induce humoral (immunoglobulin A [IgA]) and cellular immunity.<sup>2</sup> Moreover, in in vitro culture of muscle cells, the S protein caused a cytokine storm and oxidative stress.<sup>3</sup>

Coronaviruses replicate and synthesise structural proteins inside host cells. To enter the host cell, the S glycoprotein binds to the host receptor, angiotensin-converting enzyme 2 (ACE2).<sup>2</sup> Host cell proteases (mainly the transmembrane serine protease [TMPRSS2]) activate the S protein and cleave it into the ACE2-binding S1 subunit and the S2 subunit involved in membrane anchoring of the S protein and virus–host cell membrane fusion. This leads to chronic activation of the renin–angiotensin–aldosterone system (RAAS) and inflammation, apoptosis, fibrosis, the release of antidiuretic hormone and aldosterone, and water and sodium retention.<sup>1</sup>

The S protein determines tissue tropism and host selection.<sup>2</sup> The target of SARS-CoV-2 is cells of the nasal cavity that express ACE2 on the surface, enabling endocytosis, including sustentacular cells, microvilli cells, Bowman’s gland cells, basal cells and pericytes.<sup>4,5</sup> During SARS-CoV-2 infection, nasal epithelial cells undergo necroptosis and uncontrollably release cytokines – chemokines, pro-inflammatory factors and interferons – a phenomenon called the cytokine

storm. This response aims to oppose viruses and to recruit immune cells.<sup>6</sup> Moreover, the well-vascularised nasal septum is a source of leucocytes that recognise viral antigens and enhance inflammation.<sup>7</sup> A long-lasting cytokine storm leads to the production of reactive oxygen species (ROS), and the nasal epithelium becomes thin and patchy (epithelial exfoliation), with fewer cilia, supporting cells and olfactory receptors.<sup>8</sup> Damage to the nasal cavity and mucosal dryness are cumulative and may lead to greater susceptibility to pathogens in the future.<sup>4,9</sup>

Polyhydroxylated C<sub>60</sub> fullerene (fullerenol) is an allotropic form of carbon consisting of carbon, oxygen and hydrogen arranged in a truncated icosahedron. A single particle is 1 nm and resembles a football in shape.<sup>10</sup> Fullerenes are formed as natural products during combustion. In the laboratory, C<sub>60</sub> is most often created by electric arc discharge.<sup>11</sup> In turn, fullerenol is produced as a result of nitration of fullerene and the substitution of OH for NO<sub>2</sub>.<sup>12</sup> The high electro-negativity of fullerenes resulting from the large number of delocalised  $\pi$  double bonds means that they can accept electrons and neutralise ROS and reactive nitrogen species. In this way, fullerene and its derivatives suppress intracellular oxidative stress.<sup>13</sup> The redox properties, toxicity and reactivity of fullerenols depend on the number of oxygen substituents, their arrangement and the dose used. The mechanism of C<sub>60</sub> cytotoxicity involves inhibition of tyrosine kinase activity.<sup>14</sup> Intranasal administration of C<sub>60</sub> with a diameter of 50 nm to mice and rats at a concentration of 2 mg/m<sup>3</sup> for 13 weeks increased the level of cytokines in the lungs but did not cause systemic effects.<sup>11</sup> In another study, polyhydroxylated fullerenols administered intratracheally to rats accumulated in the lungs, but only doses above 5 mg per rat induced a pulmonary inflammatory response as measured by oxidative stress and cytokine expression in the bronchoalveolar fluid.<sup>15</sup> The dose-dependent potential of fullerenol to induce lung damage suggested that fullerenol may be used in the future as an inhaled drug, but only in the short term. Fullerenol in one treatment cycle at a dose of 1 mg per rat does not agglomerate and is well distributed in the lungs, which protects against recognition and absorption by macrophages.<sup>15</sup> Jiao et al<sup>16</sup> reported the opposite results: fullerenol had anti-inflammatory effects and inhibited the migration of tendon cells in a rat model of tendinopathy.

Ectoine – (S)-1,4,5,6-tetrahydro-2-methyl-4-pyrimidinecarboxylic acid – is a natural product of bacterial origin and an extremolyte. Extremolytes act through a “preferential exclusion” mechanism, which means that they are preferentially excluded from the water–protein interface.<sup>17</sup> Halophilic and halotolerant bacteria, including representatives of *Actinobacteria*, *Firmicutes* and *Proteobacteria*, synthesise ectoine in combination with a 5-hydroxyl derivative. Ectoine is synthesised in a high-salinity environment and is released outside the cell after the bacteria have been transferred to a low-salinity environment. Ectoine inside bacterial cells protects against salinity by removing salt from the cytoplasm to ensure osmotic balance and to strengthen the stability of enzymes. In addition, ectoine protects against ultraviolet (UV) radiation and therefore has proven anti-ageing and skin barrier protective properties. In the nasal cavity, ectoine inhibits inflammation by physically protecting the mucous membrane and moisturising it. Ectoine creates a protective water coat on the surface of the mucous membranes to block the entry of allergens, viruses and bacteria while stabilising the mucous membranes and protecting against structural changes and water loss. Viruses can be trapped in the water coat and then removed by washing and/or blowing the nasal cavity. In this way, ectoine has a proven effect on the regression of nasal allergy symptoms such as runny nose, itching, mucosal congestion and sneezing, as well as the symptoms of rhinosinusitis such as nasal obstruction, nasal discharge, headache, disturbance of smell/taste and others.<sup>18</sup> The cessation of the severity of the above-mentioned symptoms is comparable to the use of xylometazoline, glucocorticoids and antihistamines, with a high safety profile.

This article documents preclinical research on the development of a potential intranasal medical device containing fullerenol and ectoine. First, we characterised this novel fullerenol–ectoine composite. We then assessed its toxicity to primary human nasal epithelial cells (HNEpCs). Finally, we assessed the ability of this composite to physically block the interaction between the S protein or its RBD and the HNEpC membrane, as assessed by the expression of inflammatory mediators.

## Materials and Methods

### Characterisation of C<sub>60</sub>(OH)<sub>40</sub> and Ectoine

Polyhydroxylated fullerene C<sub>60</sub> nanoparticles were obtained from US Research Nanomaterials, Inc. (CASRN 99685-96-8, Houston, TX, USA). The starting material for the synthesis of nanoparticles was fullerene C<sub>60</sub> with a purity of >99%.

Polyhydroxylated fullerene was created as a result of the functionalisation of fullerene with 40 hydroxyl groups. The solubility of polyhydroxylated fullerene in water is 5 g/100 mL. The nanoparticles were in the form of a dark brown powder, which was dissolved in ultrapure water to a working concentration of 10,000 mg/L. The concentrated solution was diluted to 10, 50 and 100 mg/L and stored at 4°C.

Ectoine (Mw = 142.2 g/mol) in the form of a white powder and with  $\geq 95.0\%$  purity (high-performance liquid chromatography [HPLC]) was purchased from Sigma-Aldrich (No. 81619-1G-F, St. Louis, MO, USA). According to the manufacturer's data sheet, the source of ectoine was the bacterium *Halomonas elongata*. The solubility of ectoine in water is 4.0 mol/L. The powder was dissolved in ultrapure water to a working concentration of 10%. The concentrated solution was then diluted to 0.2%, 1% or 2%.

Polyhydroxylated fullerene  $C_{60}(OH)_{40}$  nanoparticles at a concentration of 10 mg/L were sonicated in an ultrasonic bath (Bandelin Electronic, Berlin, Germany) for 15 min before their characterisation. The zeta potential of 10 mg/L nanoparticles, 0.2% ectoine and their composite was measured in triplicate using a Nano-ZS90 Zetasizer (Malvern Instruments, Malvern, UK). The composite was prepared in water, maintaining a final concentration of 10 mg/L for  $C_{60}(OH)_{40}$  and 0.2% for ectoine. A Nano-ZS90 Zetasizer was used for dynamic light scattering. The shape, size and distribution of  $C_{60}(OH)_{40}$  nanoparticles alone and in the fullerene–ectoine composite were determined by dropping 5  $\mu\text{L}$  of the colloid on copper grids for transmission electron microscopy (TEM; JEM-1220 JEOL, Tokyo, Japan).

The elemental composition of the surface of fullerene, ectoine and their composite was analysed using attenuated total reflectance–Fourier transform infrared (ATR–FTIR) spectroscopy and energy-dispersive X-ray spectroscopy (EDS). All the samples were prepared by adding 200  $\mu\text{L}$  of the colloid onto a glass slide and drying in an Avantgarde Line Series ED dryer (Binder GmbH, Tuttlingen, Germany). The following samples were prepared: fullerene at a concentration of 0.1%, ectoine at a concentration of 10% and a composite with a final concentration of fullerene 500 mg/L and ectoine 10%. FTIR spectra were recorded using a Tensor 27 FTIR–ATR (Bruker Corporation, Ettlingen, Germany) with a IS50 ATR (Thermo Fisher Scientific, Waltham, MA, USA) from 4500 to 400  $\text{cm}^{-1}$  with a resolution of 4  $\text{cm}^{-1}$  and 64 scans. Each side of the sample was measured four times. The background spectrum – that is, water vapor and carbon dioxide present in the air – was removed. FTIR spectra were generated using the OriginPro 2024 version 10.1.0.170 software (OriginLab Corporation, Northampton, MA, USA). The chemical composition was also determined by using a second a Quanta FEG 250 scanning electron microscope combined with an EDAX DX4 for EDS microanalysis; this method has a lower detection limit of  $<0.1\%$  per element. Samples were recorded at 10 different locations in triplicate.

NanoDrop™ One/OneC Microvolume UV-Vis Spectrophotometer (Thermo Fisher Scientific, Waltham, MA, USA) was used to determine the transmittance of electromagnetic radiation with a wavelength between 180 and 850 nm in samples. Two microliters of 10 mg/L fullerene, 0.2% ectoine and their composite were added to the nanodrop and three measurements were performed each. The measured light transmittance was then converted to an absorbance measurement using the Beer–Lambert law equation. Surface plasmon resonance provided indirect information about the size and shape of materials.

## HNEpC Culture

HNEpCs, which were originally isolated from normal human nasal mucosa, were purchased from PromoCell (No. C-12620, Heidelberg, Germany). After thawing, HNEpCs were cultivated under standard conditions (37°C, 5%  $\text{CO}_2$  and 95% relative humidity) in Airway Epithelial Cell Growth Medium (No. C-21160, Sigma-Aldrich) containing bovine pituitary extract (0.004 mL/mL), epidermal growth factor (10 ng/mL), insulin (5  $\mu\text{g}/\text{mL}$ ), hydrocortisone (0.5  $\mu\text{g}/\text{mL}$ ), epinephrine (0.5  $\mu\text{g}/\text{mL}$ ), triiodo-L-thyronine (6.7 ng/mL), transferrin (10  $\mu\text{g}/\text{mL}$ ) and retinoic acid (0.1 ng/mL). The culture medium was replaced every 2–3 days. HNEpCs were maintained at the recommended planting density 10,000 cells/ $\text{cm}^2$ . Cells were detached from culture flasks when they reached 70–90% confluence using DetachKit (No. C-41200, Sigma-Aldrich), which contains HEPES-buffered balanced salt solution (BSS), trypsin/ethylenediaminetetraacetic acid (EDTA) solution (0.04%/0.03%) and trypsin neutralisation solution. HEPES BSS contains 30 mm HEPES, D-Glucose, NaCl, KCl, sodium phosphate and phenol red. Trypsin neutralisation solution contains 0.05% trypsin inhibitor from soybean and 0.1% bovine serum albumin (BSA). Trypsinisation was performed at room temperature. Cells were stored in Cryo-SFM (No. C-29910, Sigma-Aldrich) in liquid nitrogen. Cryo-SFM is a freezing medium that contains

methylcellulose, dimethyl sulfoxide (DMSO) and other cryoprotectants for the cryopreservation of human and animal primary cells.

## Effect of C<sub>60</sub>(OH)<sub>40</sub>, Ectoine and Their Composite on HNEpC Viability

HNEpCs were seeded in 6- and 96-well plates at the recommended testing density of  $1.5 \times 10^5$  and  $1.5 \times 10^4$  cells/well, respectively. After incubation for 24 h, when the cells had adhered to the plates, the culture medium was replaced with a new medium containing the factors of interest. There were 10 groups: (1) the control group; (2) 10 mg/L C<sub>60</sub>(OH)<sub>40</sub>; (3) 50 mg/L C<sub>60</sub>(OH)<sub>40</sub>; (4) 100 mg/L C<sub>60</sub>(OH)<sub>40</sub>; (5) 0.2% ectoine; (6) 1% ectoine; (7) 2% ectoine; (8) 10 mg/L C<sub>60</sub>(OH)<sub>40</sub> and 0.2% ectoine (MIX low); (9) 50 mg/L C<sub>60</sub>(OH)<sub>40</sub> and 1% ectoine (MIX medium); and (10) 100 mg/L C<sub>60</sub>(OH)<sub>40</sub> and 2% ectoine (MIX high). The concentrations presented above are the final concentrations after dilution in Airway Epithelial Cell Growth Medium (v/v). Cells were cultured for 24 h before being used for the assays.

### (2,3-Bis-(2-Methoxy-4-Nitro-5-Sulphophenyl)-2h-Tetrazolium-5-Carboxanilide) (XTT) Assay

The Cell Proliferation Kit II (XTT, Roche, Mannheim, Germany) was used to quantify cell proliferation and viability. XTT is converted to soluble formazan by succinate dehydrogenase. The XTT labelling and electron-coupling reagents were thawed in a water bath at 37°C. Then, 5 mL of the XTT labelling reagent and 0.1 mL of the electron coupling reagent were mixed immediately before use. Cells were cultured and treated as described in the “Effect of C<sub>60</sub>(OH)<sub>40</sub>, ectoine and their composite on HNEpC viability” section. Briefly, 50 µL of the XTT labelling mixture (final concentration 0.3 mg/mL) was added to each well of a 96-well plate containing cells in 100 µL of culture medium (the blank wells contained only culture medium). After incubation for 1 and 24 h in a humidified atmosphere at 37°C and 5% CO<sub>2</sub>, the absorbance was measured at 475 nm using an Infinite 200 microplate reader (Tecan, Durham, NC, USA). The absorbance from the blank wells was subtracted. Cell viability was determined as the average of triplicates and is expressed relative to control (%).

### Morphology of Cells After May–Grünwald Giemsa (MGG) Staining

After incubation for 24 h, HNEpCs were washed with phosphate-buffered saline (PBS) containing Ca<sup>2+</sup> and Mg<sup>2+</sup> (No. P4417, Sigma-Aldrich) and then stained with the MGG method (which includes azure, methylene blue and eosin). Cells were stained for 3 min with May–Grünwald stain (No. 63590, Sigma-Aldrich) and for 30 min with Giemsa stain (No. 48900, Sigma-Aldrich). After Giemsa staining, excess dye was thoroughly washed out. After evaporating the PBS, five photos were taken at 10× and 20× magnification using a TI-LED inverted light microscope (Leica, Wetzlar, Germany) connected to a digital camera (Leica MC190 hD) and the LAS V4.10 software (Leica). Image analysis was performed using ImageJ 1.54d (National Institutes of Health, Bethesda, MD, USA).

### Morphology of Cells After Periodic Acid–Schiff (PAS) Staining

The Periodic Acid–Schiff (PAS) Staining System (No. 395B-1KT, Sigma-Aldrich) was used to stain goblet cells, epithelial sulfomucins and sialomucins, and neutral mucus substances. Goblet cells are present in the nasal mucosa tissue; their main function is to secrete mucus. Periodic acid oxidises glycols into aldehydes. After adding Schiff's reagent, pararosaniline is released, which colours elements containing glycol purple or red.

Cells were seeded in 6-well plates and incubated as described in the “Effect of C<sub>60</sub>(OH)<sub>40</sub>, ectoine and their composite on HNEpC viability” section. The PAS staining procedure was performed as described previously.<sup>19</sup> Briefly, the cells were fixed with 4% paraformaldehyde for 10 min and then washed three times with PBS. Periodic acid solution, Schiff's reagent and haematoxylin solution were equilibrated to room temperature; the entire procedure was carried out at 22°C. HNEpCs were stained with 1% periodic acid for 5 min, Schiff's reagent for 15 min and haematoxylin for 90s. After each staining step, HNEpCs were washed with PBS. At least 10 photos were taken from different fields of view using an inverted TL-LED light microscope (Leica). Cells with purple-red cytoplasm were counted as PAS positive.

## Effect of the S Protein Concentration on HNEpC Viability

Recombinant human coronavirus SARS-CoV-2 S glycoprotein (His tag) was purchased from Abcam (No. ab281471, Cambridge, UK). It was synthesised in Chinese hamster ovary cells. The S protein was used to mimic viral infection on

the surface of the nasal mucosa. For this purpose, HNEpCs were seeded in 96-well plates at  $1.5 \times 10^4$ /well. After 24 h, Airway Epithelial Cell Growth Medium was replaced with a fresh medium containing the S protein at a concentration of 0 (control), 1, 2, 3, 4 or 5  $\mu\text{g/mL}$  culture medium.

### XTT Assay

The XTT assay kit (Roche) was used to determine the effect of the S protein on HNEpC viability. HNEpCs were transferred to a 96-well plate, and after adhesion to the plate, they were incubated for 24 h with the S protein at a concentration of 1, 2, 3, 4 or 5  $\mu\text{g/mL}$ . The XTT assay was performed as described in the “(2,3-Bis-(2-methoxy-4-nitro-5-sulfophenyl)-2h-tetrazolium-5-carboxanilide) (XTT) assay” section, the incubation time was 1 h.

### ROS Assays

One of the cellular defence mechanisms against viral infections is the production of ROS, the level of which was evaluated using 2',7'-dichlorofluorescein diacetate (DCF-DA, No. D6883, Sigma-Aldrich) and the Fluorometric Intracellular ROS Kit (No. MAK143, Sigma-Aldrich). HNEpCs were seeded in 96-well black plates and treated with various concentrations of the S protein, as described in the “Effect of the S protein concentration on HNEpC viability” section.

For the DCF-DA assay, 10 mM DCF-DA was prepared in DMSO. Next, DCF-DA was diluted in Airway Epithelial Cell Growth Medium to a concentration of 25  $\mu\text{M}$ . After the cells had been exposed to the S protein for 4 h, the culture medium was discarded, and 100  $\mu\text{L}$  of 25  $\mu\text{M}$  DCF-DA was added to each well. The cells were incubated at 37°C in the dark, and measurements at excitation and emission wavelengths of 485 and 535 nm, respectively, were taken every 5 min for a total of 25 min. Fluorescence intensity is expressed as a per cent relative to the control.

The Fluorometric Intracellular ROS Kit was used to determine the effect of incubation for 24 h with the S protein on ROS production in cells and in the culture medium. The assay was performed by following the manufacturer's instructions. First, the ROS Detection Reagent was dissolved in 40  $\mu\text{L}$  of DMSO. Then, 20  $\mu\text{L}$  of the ROS Detection Reagent was added to 10 mL of Assay Buffer to create the master reaction mix. The cell culture medium was removed, and 100  $\mu\text{L}$  of the master reaction mix was added to each well. The cell culture medium was saved to measure the ROS level; for this purpose, 50  $\mu\text{L}$  of the master reaction mix was added to 50  $\mu\text{L}$  of culture medium. Cells and culture media were incubated for 1 h in the dark. The fluorescence intensity was measured at excitation and emission wavelengths of 490 and 525 nm, respectively, using an Infinite 200 microplate reader (Tecan). Fluorescence intensity is expressed as a per cent relative to the control. The final ROS content is also expressed in relation to the viability after 24 h.

## The Ability of $\text{C}_{60}(\text{OH})_{40}$ and Ectoine to Protect HNEpCs Against the S Protein

A modified sensitivity test of cells previously treated with  $\text{C}_{60}(\text{OH})_{40}$  and ectoine to the S protein was performed (ISO PN-EN 5.5.4.2). HNEpCs were seeded on culture plates at  $2.0 \times 10^4$  cells/cm<sup>2</sup>. After incubation for 24 h, when the cells had adhered to the surface of the vessel, Airway Epithelial Cell Growth Medium was replaced with fresh medium containing the appropriate factors. After incubation for 1 h, the S protein was added at a concentration of 2  $\mu\text{g/mL}$  to the culture medium (v/v); the incubation lasted 24 h. There were five treatment groups: (1) no treatment – negative control; (2) the S protein – positive control; (3) 10 mg/L  $\text{C}_{60}(\text{OH})_{40}$  and the S protein; (4) 0.2% ectoine and the S protein; and (5) 10 mg/L  $\text{C}_{60}(\text{OH})_{40}$ , 0.2% ectoine and the S protein. A quantitative reverse transcription polymerase chain reaction (RT-qPCR) was performed using samples from groups 1, 2 and 5.

### Characterisation of the S Protein and Its Interaction with Nanoparticles

The shape and size of the S protein and its interaction with nanoparticles were assessed with TEM. The S protein alone (1  $\mu\text{g}$ ) or the S protein (1  $\mu\text{g}$ ) and fullerol (10 mg/L) and ectoine (0.2%) was dropped on a copper grid (a total volume of 5  $\mu\text{L}$ ) and examined with a JEM-1220 (JEOL, Tokyo, Japan). After drying the grids, five photos were taken at two magnifications. The zeta potential and the size of the S protein in water (0.2  $\mu\text{g/mL}$ ) were measured using a Nano-ZS90 Zetasizer (Malvern Instruments) in triplicate.

## Inverted Confocal Microscopy

HNEpCs were seeded on 35-mm  $\mu$ -Dish with a glass coverslip bottom (No. 81158, Animalab, Teltow, Germany). The next day, the culture medium was replaced with a fresh medium containing the appropriate factors as detailed in “The ability of C<sub>60</sub>(OH)<sub>40</sub> and ectoine to protect HNEpCs against the S protein” section. After incubation for 24 h, the cells were fixed in 4% paraformaldehyde in 0.1 M phosphate buffer, pH 7.2 (Sigma-Aldrich) for 10 min. The cells were washed with PBS and then permeabilised with 0.5% Tween 20 in PBS (Sigma-Aldrich) for 10 min. In the next step, the cells were incubated with PBS containing 2% goat serum, 1% BSA and 0.25% glycine (Sigma-Aldrich) for 30 min to block free protein-binding sites on the plates. The cells were incubated with 300  $\mu$ L of a rabbit anti-ACE2 antibody (No. SAB3500978, Sigma-Aldrich, St. Louis, MO, USA) diluted to 1:100 in 1% BSA overnight at 4°C. The next day, the cells were washed three times with PBS and then incubated with 300  $\mu$ L of goat anti-rabbit IgG (H+L) secondary antibody conjugated to Alexa Fluor 555 (No. A32732, Thermo Fisher Scientific) diluted 1:200 in blocking solution for 3 h at room temperature. The cells were washed three times with PBS and then stained with 5  $\mu$ M 4',6-diamidino-2-phenylindole (DAPI, No. ab228549, Abcam) for 15 min. After rinsing with PBS, the Ividi Mounting Medium (No. 50001, Animalab, Teltow, Germany) was used to cover the dishes. The cells were observed at 10 $\times$  and 40 $\times$  magnification using an IX 81 FV-1000 confocal microscope (Olympus Corporation, Tokyo, Japan).

## Human Inflammation Antibody Array

Inflammatory cytokines in the HNEpC culture medium were assessed using the Human Inflammation Antibody Array (ab134003, Abcam), which includes a set of 40 antibodies. Culture medium was collected as described previously, centrifuged at 1600 rpm for 5 min and then used for the array, which was performed according to the manufacturer's instructions. Briefly, after blocking the membrane with 1 $\times$  blocking buffer for 30 min at 22°, 1 mL of undiluted culture medium was added; the membrane was incubated overnight at 4°C. Following washing, the membrane was incubated with 1 mL of biotin-conjugated antibodies for 24 h at 4°C. After washing again, the membrane was incubated with 2 mL of horseradish peroxidase-conjugated streptavidin for 2 h at room temperature. Following the final wash, the membrane was visualised with Azure c400 (Azure Biosystems, Dublin, CA, USA). Exposure times of 30s to 5 min were used. ImageJ 1.54d (National Institutes of Health, Bethesda, MD, USA) was used for semi-quantitative analysis of the membrane using the Protein Array Analyzer.

## RT-qPCR

### RNA Isolation

RNA was isolated from HNEpCs in groups 1, 2 and 5, as described in “The ability of C<sub>60</sub>(OH)<sub>40</sub> and ectoine to protect HNEpCs against the S protein” section, using the PureLink RNA Mini Kit (Invitrogen, Waltham, MA, USA) according to the manufacturer's protocol. Briefly, the culture medium was removed, and the cells were washed with PBS and detached with trypsin. The cells were collected by centrifugation at 1600 rpm and lysed in a lysis buffer containing 1% 2-mercaptoethanol. Then, 70% ethanol was added to the lysate in a 1:1 ratio; the lysate was transferred to the spin cartridge with a collection tube and centrifuged for 15s at 12,000 g. RNA was purified using wash buffers I and II. RNA was eluted by adding 40  $\mu$ L of RNase-free water to the dried spin cartridge and centrifuging for 1 min. at 12,000 g. The RNA concentration and purity were checked using NanoDrop™ One/OneC Microvolume UV-Vis Spectrophotometer (Thermo Fisher Scientific). The RNA concentration was adjusted to 1000 ng/10  $\mu$ L (100 ng/ $\mu$ L).

### Reverse Transcription

The isolated RNA was reverse transcribed into complementary DNA (cDNA) with the cDNA High Capacity Reverse Transcription Kit (Applied Biosystems, Foster City, CA, USA). Each reaction comprised 2  $\mu$ L of RT buffer, 0.8  $\mu$ L of the dNTP mix, 2  $\mu$ L of random primers, 1  $\mu$ L of reverse transcriptase, 4.2  $\mu$ L of RNase-free water and 10  $\mu$ L of isolated RNA. A 2720 thermal cycler (Thermo Fisher Scientific) was used for reverse transcription with the following temperature programme: 25°C for 10 min, 37°C for 120 min and 85°C for 5 min. The cDNA concentration was measured using a NanoDrop™ One/OneC Microvolume UV-Vis Spectrophotometer (Thermo Fisher Scientific).

### RT-qPCR

Each qPCR included 5 µL of cDNA (100 ng) and 10 µL of the reaction mixture (0.75 µL of forward primer, 0.75 µL of reverse primer, 7.5 µL of Syber Green Master Mix, Thermo Fisher Scientific, and 1 µL of water). Lyophilised primers were purchased from Genomed (Warsaw, Poland) and then reconstituted at a concentration of 10 µM. The sequences of the primers used are listed in Table 1. A StepOnePlus™ Real-Time PCR System (Applied Biosystems) was used for qPCR, with the following temperature programme: 95°C for 10 min, followed by 40 cycles of 95°C for 15s and 60°C for 60s. Each sample was run in quadruplicate. Relative gene expression was determined according to the  $2^{-\Delta\Delta CT}$  method, using the formulae  $\Delta CT = CT_{\text{gene}} - CT_{\text{GAPDH}}$  and  $-\Delta\Delta CT = -(\Delta CT_{\text{gene}} - \Delta CT_{\text{control}})$ .

### Statistical Analysis

The data were analysed with one-way analysis of variance (ANOVA) followed by the Bonferroni post hoc test using GraphPad Prism 8.0.2 (GraphPad Software, San Diego, CA, USA). The results are presented as the mean and standard deviation of three replicates. The results were considered statistically significant when  $p \leq 0.05$ . In the figures, asterisks indicate the levels of significance: (\*)  $p \leq 0.05$ ; (\*\*)  $p \leq 0.01$  and (\*\*\*)  $p \leq 0.001$ .

## Results

### Ectoine Increased the Stability of the Composite, Was a Source of Nitrogen and Protected Against the Agglomeration of Fullerenol Nanoparticles

The spectra recorded by the Zetasizer showed two peaks for fullerenol nanoparticles: 79.6 and 612.8 nm (Figure 1A). The fullerenol spectrum changed after the addition of ectoine: there were still two peaks, but at notably smaller sizes, namely 68.76 and 297.1 nm (Figure 1B). The average hydrodynamic size and polydispersity of fullerenol nanoparticles were  $768.9 \pm 6.45$  nm and  $0.691 \pm 0.03$ , respectively. Interestingly, after the incubation of fullerenol nanoparticles with ectoine, their average size was much lower ( $347.63 \pm 62.31$  nm; Figure 1C). However, the addition of ectoine did not affect the polydispersity of the nanoparticles, which was  $0.67 \pm 0.10$ . Fullerenol nanoparticles formed unstable

**Table 1** Nucleotide Sequences of the Primers Used to Determine the Expression of Genes Associated with Severe Acute Respiratory Syndrome Coronavirus 2 (SARS-CoV-2) Infection

Gene	Primer Sequence (5' → 3')	Amplicon Size (Base Pairs)	GenBank Accession Number
Angiotensin-converting enzyme (ACE2)	F: TCCATTGGTCTTCTGTCACCCG R: AGACCATCCACCTCCAATTCTC	133	NM_001389402.1
Monocyte chemoattractant protein 1 (MCP-1)	F: AGAATCACCAGCAGCAAGTGTCC R: TCCTGAACCCACTTCTGCTTGG	98	NM_002982.4
Interleukin 6 (IL-6)	F: ATGAACTCCTTCTCCACAAGCGC R: GAAGAGCCCTCAGGCTGGACTG	628	XM_054358146.1
Tissue inhibitor of metalloproteinases 2 (TIMP-2)	F: ACCCTCTGTGACTTCATCGTGC R: GGAGATGTAGCACGGGATCATG	129	NM_003255.5
Intercellular adhesion molecule (ICAM)	F: AGCGGCTGACGTGTGCAGTAAT R: TCTGAGACCTCTGGCTTCGTCA	115	NM_000201.3
Interleukin 8 (IL-8)	F: GAGAGTGATTGAGAGTGGACCAC R: CACAACCCTCTGCACCCAGTTT	112	NM_001354840.3
Glyceraldehyde-3-phosphate dehydrogenase (GAPDH)	F: GAGAAGGCTGGGGCTCATTTG R: CATGGTTCACCCCATG	97	NM_002046



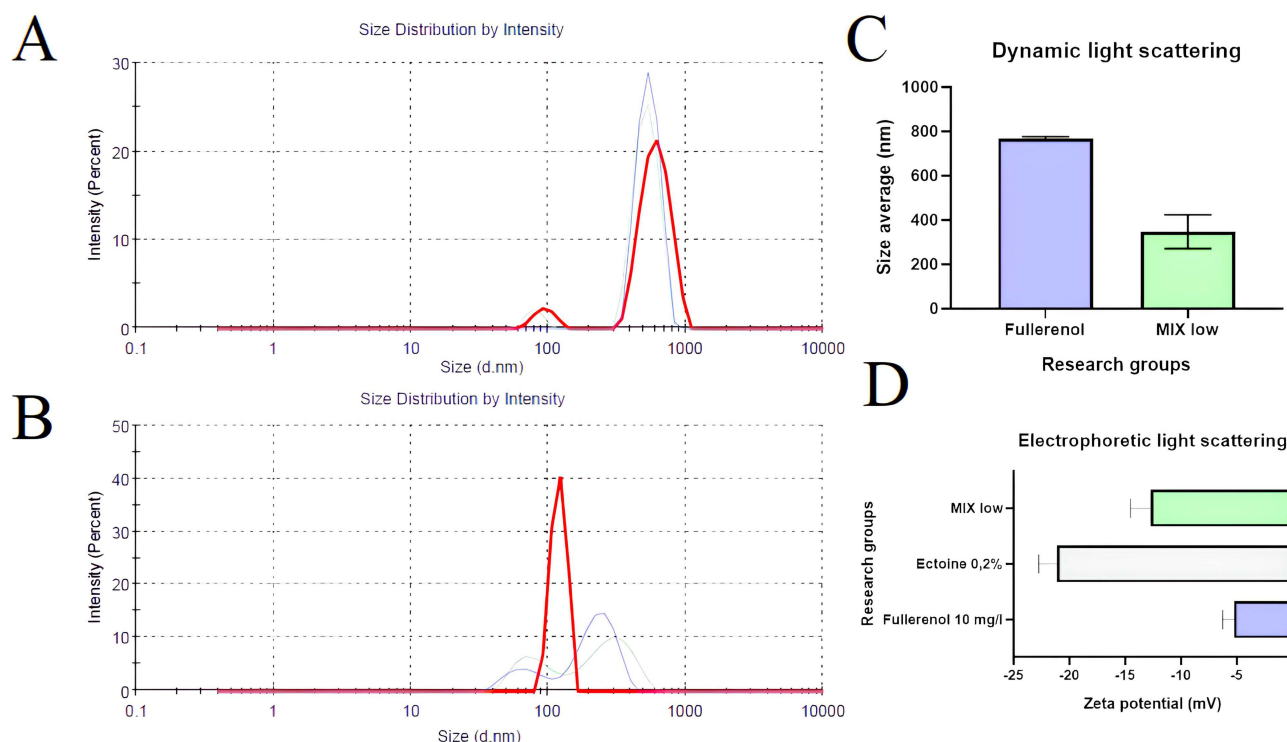


**Figure 1** Characterisation of fullerene nanoparticles at a concentration of 10 mg/L. **(A)** Size distribution of fullerene nanoparticles suspended in water. **(B)** Size distribution of fullerene nanoparticles in water containing 0.2% ectoine. **(C)** Average size of fullerene nanoparticles in water and in water containing 0.2% ectoine (MIX low). **(D)** Zeta potential of fullereneol, ectoine and their composite (MIX low).

agglomerates with a zeta potential of  $-5.26 \pm 0.82$  mV, which increased to  $-12.73 \pm 1.46$  mV after adding ectoine. The zeta potential of the aqueous solution of 2% ectoine was  $-21.1 \pm 1.34$  mV (Figure 1D).

Based on TEM, fullerene nanoparticles formed irregularly shaped clusters ranging in size from 25 to 480 nm (Figure 2A). The addition of ectoine to fullerene loosened the clusters, and there were round structures with a diameter of up to several nanometres on their edges.

We scanned fullereneol, ectoine and the fullereneol–ectoine composite using FTIR spectroscopy, between 500 and 4000  $\text{cm}^{-1}$  (Figure 2B). The fingerprint region of the FTIR spectra ( $<1400$   $\text{cm}^{-1}$ ) contained several peaks, but they were difficult to assign, as previously reported by Tanne et al.<sup>20</sup> We noted two distinct bands in this area (500 and 900  $\text{cm}^{-1}$ ). In fullereneol, there were weak bands at 1400 and 1380  $\text{cm}^{-1}$  as a result of stretching of the C-O and C-H groups. The band at 1625  $\text{cm}^{-1}$  resulted from the presence and vibration of double carbon bonds, and the band at 2350  $\text{cm}^{-1}$  was from triple carbon bonds. From 3200 to 2600  $\text{cm}^{-1}$  there were two clearly visible bands corresponding to C-H stretching vibrations from chain hydrocarbons (2910 and 2950  $\text{cm}^{-1}$ ) and one faintly visible C-H band from the C<sub>60</sub> ring ( $>3000$  -  $\text{cm}^{-1}$ ). The broad band, located on the right side of the spectrum, was from the vibrations of OH groups from water and OH attached to carbon. The arrows in Figure 2B show the water group (3500  $\text{cm}^{-1}$ ) and the alcohol-like group (3350  $\text{cm}^{-1}$ ). For ectoine, we observed clearly visible bands at 1380 and 1400  $\text{cm}^{-1}$  due to stretching of the C-H and C-O groups. The structured, very strong band at 1625  $\text{cm}^{-1}$  was from the stretching of carbon double bonds in ectoine. There was also a carbon triple bond band at 2350  $\text{cm}^{-1}$ . The ectoine FTIR spectrum showed a distinct additional band that was absent from the fullereneol spectrum, namely the NH stretching region at  $>2500$   $\text{cm}^{-1}$ . Further, at  $<3050$   $\text{cm}^{-1}$ , there were as many as five bands corresponding to C-H functional groups (2830, 2870, 2910, 2950 and 3050  $\text{cm}^{-1}$ ). There was an OH stretching vibration band at 3350  $\text{cm}^{-1}$ . The fullereneol–ectoine composite FTIR spectrum showed most of the features of the ectoine spectrum due to the predominance of ectoine in the mixture. However, the composite showed lower transmittance and higher absorption of infrared radiation compared with the ectoine FTIR spectrum at the same wavelengths.

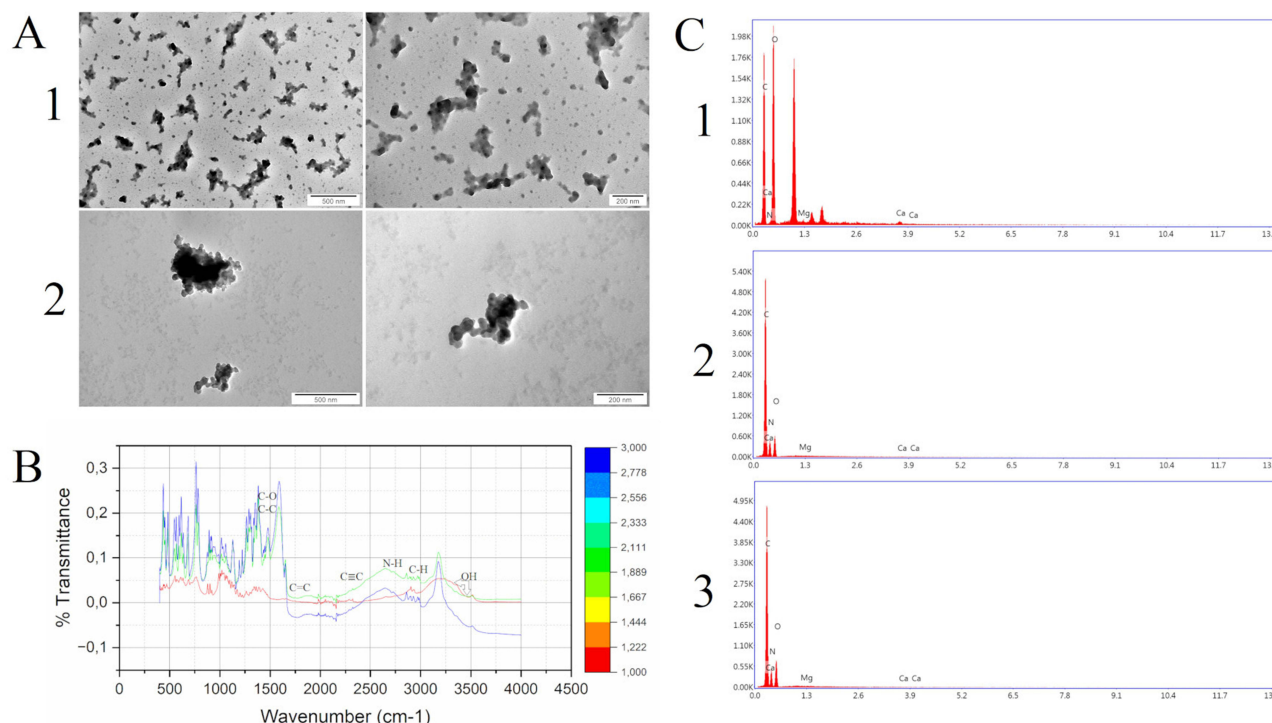


**Figure 2** (A) Morphology of (1) fullerene C<sub>60</sub>(OH)<sub>40</sub> nanoparticles and (2) fullerene C<sub>60</sub>(OH)<sub>40</sub> nanoparticles together with ectoine viewed under a transmission electron microscope. The scale bar is 500 nm (left side) and 200 nm (right side). (B) Characterisation of the surface chemistry of fullerene using Fourier-transform infrared spectroscopy. The different colours of the lines indicate the groups: red for fullerene, green for ectoine and blue for the fullerene–ectoine composite (MIX low). (C) Energy-dispersive spectroscopic results for elemental composition of (1) fullerene C<sub>60</sub>(OH)<sub>40</sub>, (2) ectoine and (3) their composite.

We analysed the chemical composition of thin layers of fullerene, ectoine and the fullerene–ectoine composite by using EDS (Table 2). The spectra in Figure 2C show that, as expected, carbon (39.79%) and oxygen (58.65%) were the main components of fullerene C<sub>60</sub>(OH)<sub>40</sub>. Interestingly, we noted nitrogen in the fullerene spectrum (0.83%). The carbon, oxygen and nitrogen weight concentration in the ectoine spectrum was 47.14%, 19.58% and 33.12%, respectively. The fullerene–ectoine composite with a mass ratio of 1:200 presented the highest mass share of carbon (45.5%). Given the largest share of ectoine in the composite, elemental analysis showed a clear mass increase in nitrogen (31.45%) and a decrease in oxygen (22.85%) compared with fullerene alone. Moreover, there were additional peaks of trace elements with a mass concentration of <0.4%, including magnesium and calcium, which may have resulted from sample contamination during preparation or occurred during the synthesis stage.

**Table 2** Energy-Dispersive Spectrometry Results of Primary Human Nasal Epithelial Cells (HNEpCs) Treated with Fullerene C<sub>60</sub>(OH)<sub>40</sub>, Ectoine or Their Composite (MIX Low)

Research Group	Element	wg%	at%
Fullerene C <sub>60</sub> (OH) <sub>40</sub>	C	39.79	46.91
	N	0.83	0.84
	O	58.65	51.91
	Mg	0.36	0.21
	Ca	0.36	0.13

(Continued)

**Table 2** (Continued).

Research Group	Element	wg%	at%
Ectoine	C	47.14	52.20
	N	33.12	31.44
	O	19.58	16.27
	Mg	0.15	0.08
	Ca	0.01	0.00
MIX low	C	45.50	50.71
	N	31.45	30.05
	O	22.85	19.12
	Mg	0.20	0.11
	Ca	0.00	0.00

The UV–Vis spectrum analysis revealed some important features. The spectrum of fullereneol showed a characteristic, broad peak in the range of 180–300 nm. However, the absorbance maximum for fullereneol was located at 249 nm. The spectrum of ectoine had one characteristic and narrow peak at 225 nm. Additionally, the UV–Vis spectrum of the composite was similar to the ectoine peak (Figure 3).

### The Fullereneol–Ectoine Composite Was Not Toxic to HNEpCs After Incubation for 24 h and Caused Cytotoxicity After 48 h

The XTT assay results regarding the effect of different concentrations of fullereneol, ectoine and their composite on HNEpCs are presented in Figure 4. All fullereneol  $C_{60}(OH)_{40}$  and fullereneol–ectoine composite concentrations were not

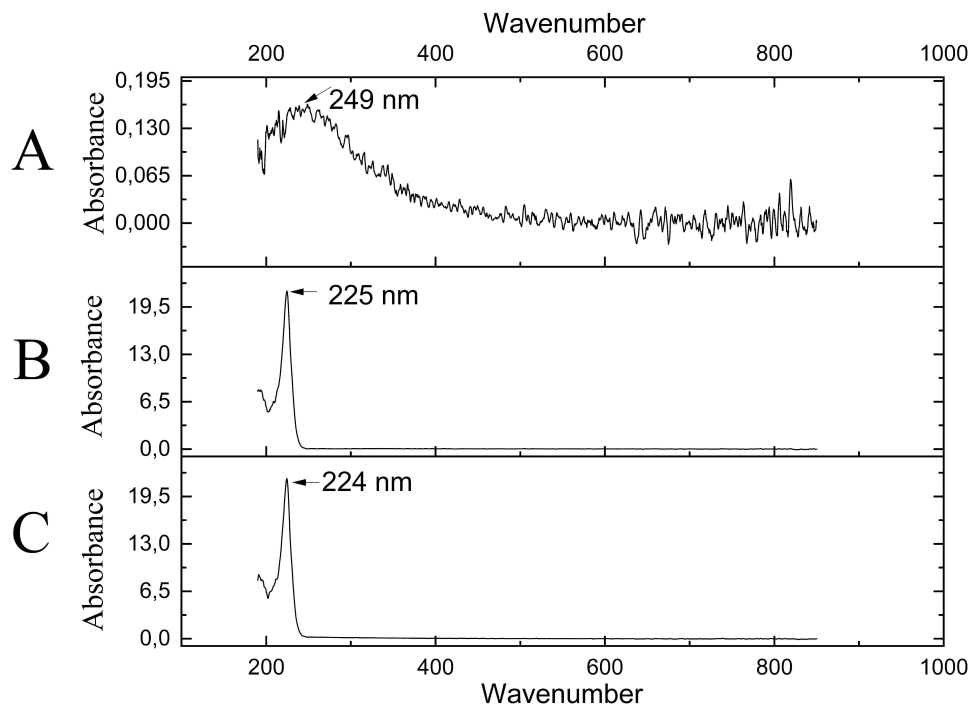


**Figure 3** UV-Vis of 10 mg/L fullereneol (A), 0.2% ectoine (B) and their composite (C). Arrows indicate the absorbance maximum in the wavelength range 180–850.

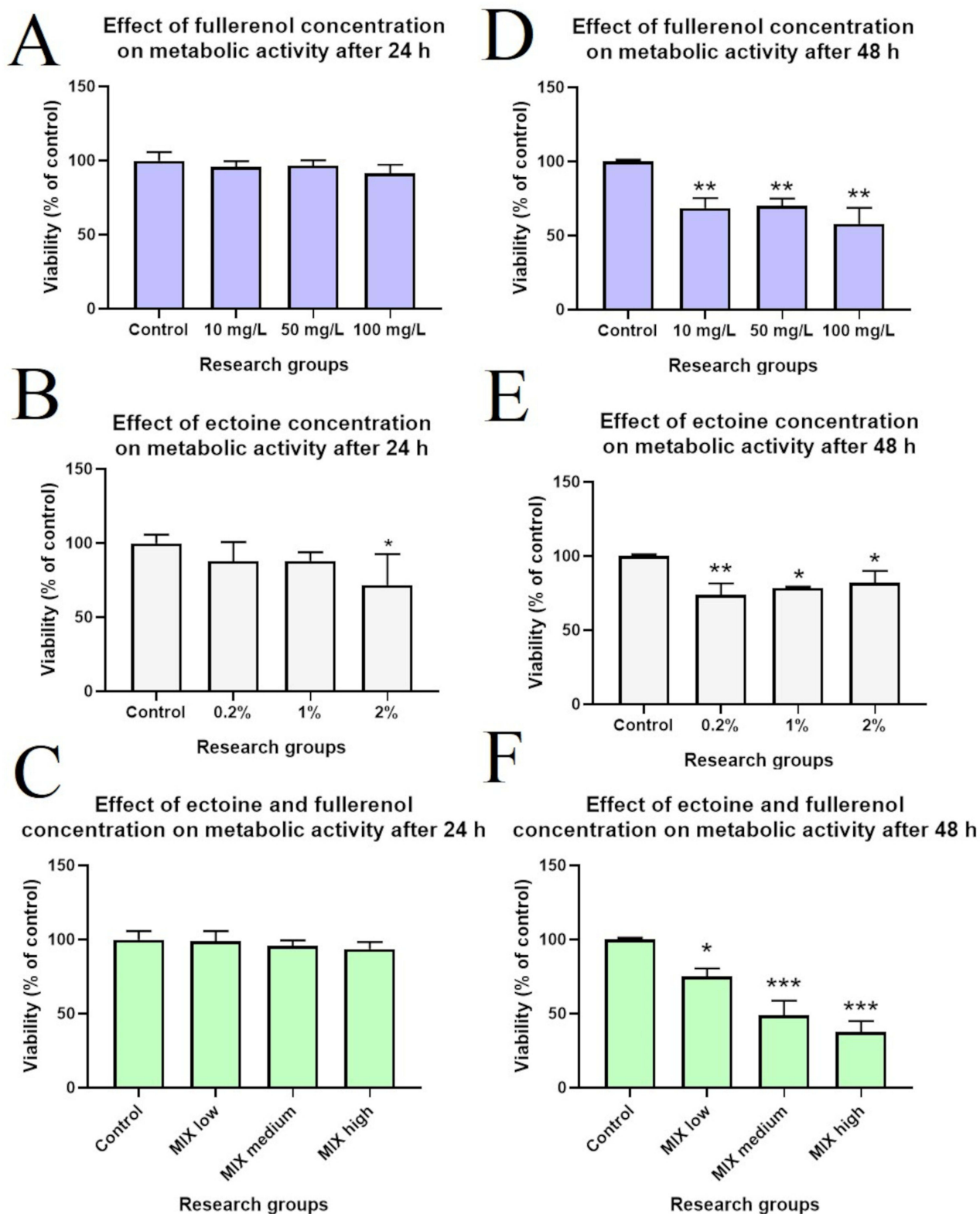


**Figure 4** Succinate dehydrogenase activity of primary human nasal epithelial cells (HNEpCs) after incubation for (A–C) 24 h and (D–F) 48 h with fullerene  $C_{60}(OH)_{40}$ , ectoine and their composites measured with the XTT assay. MIX low is 10 mg/L of fullerene and 0.2% of ectoine; MIX medium is 50 mg/L of fullerene and 1% of ectoine; MIX high is 100 mg/L of fullerene and 2% of ectoine. In the figure, asterisks indicate the level of significance: (\*)  $p \leq 0.05$ ; (\*\*)  $p \leq 0.01$  and (\*\*\*)  $p \leq 0.001$ .

toxic to these cells when incubated for 24 h. Incubation with 0.2% or 1% ectoine for 24 h was not toxic to HNEpCs; however, 2% ectoine significantly reduced cell viability to 71.9% ( $p = 0.0296$ ). After incubation for 48 h, all tested fullereneol and ectoine concentrations significantly reduced HNEpC viability. HNEpC viability was most strongly reduced in the group treated with 100 mg/L fullereneol or 0.2% ectoine. Among the tested fullereneol–ectoine composites, the most biocompatible contained 0.2% ectoine and 10 mg/L fullereneol (MIX low), which led to a 25% reduction in viability compared with the control group ( $p = 0.0249$ ). There was a much more pronounced reduction in viability for the MIX medium (51%,  $p = 0.0007$ ) and MIX high (62%,  $p = 0.0004$ ) groups.

## The Fullereneol–Ectoine Composite Increased Intracellular Adhesion Characteristics of HNEpCs

We assessed the morphology of HNEpCs with MGG staining. The control group showed the typical HNEpC morphology, namely a cobblestone pattern. The HNEpCs coculture consisted of cells of various sizes, from several to several dozen micrometres, which resulted from the different types of cells in the culture. Cells used for the experiments were from passages 1 to 4.

Fullereneol at 10 mg/L and 50 mg/L was not toxic to HNEpCs and did not affect their morphology (Figure 5, Table 3). In particular, higher fullereneol concentration (100 mg/L) resulted in the formation of tight cell clusters and a decrease in the cell nuclei number per square millimeter of the growth surface. However, the quantitative morphological analysis showed no differences in the total cell surface area after the addition of fullereneol independent of concentration.

Ectoine did not induce drastic changes in HNEpC morphology (Figure 6). The cells resembled control cells in appearance, but the population of cells with large cell bodies was reduced regardless of the ectoine concentration. All ectoine concentrations loosened intercellular connections. Compared with the control group, the number of HNEpCs and cell covered area (%) were similar after the addition of 0.2%, 1% and 2% ectoine (Table 3).

Regarding the fullereneol–ectoine composite, MIX low did not significantly change HNEpC morphology, but there were more multicellular clusters. MIX medium or MIX high resulted in the formation of large cell clusters in which individual cells were smaller in size than in the control group and occupied less space. However, the addition of the fullereneol–ectoine composites did not reduce the number of cells compared with the control group (Figure 7, Table 3).

We also performed PAS staining to determine the effect of ectoine and fullereneol on mucus secretion by HNEpCs. Compared with the control group, the addition of fullereneol did not alter the intensity of cytoplasmic staining. HNEpCs exposed to 10 mg/L fullereneol grew singly, similarly to the control group. However, the addition of 50 or 100 mg/L fullereneol led to the formation of HNEpC clusters (Figure 8).

The addition of 0.2% ectoine did not change the number of mucus-secreting cells. However, the number of PAS-positive cells decreased after the addition of 1% or 2% ectoine (Figure 9).

For the fullereneol–ectoine composite, incubation with MIX low or MIX medium did not alter cytoplasmic staining. However, MIX high resulted in weaker staining. Cells were scattered in the control group and formed smaller (MIX low) or larger (MIX medium and MIX high) clusters when incubated with the composite (Figure 10).

Based on the XTT assay results and morphological assessment, we selected 0.2% ectoine, 10 mg/L fullereneol and the composite of these two concentrations for the subsequent experiments.

## The S Protein Was Cytotoxic to HNEpCs and Induced ROS Production

We evaluated the effect of the full-length recombinant S protein on HNEpC survival and ROS production by adding the S protein to the culture medium (1, 2, 3, 4 or 5  $\mu\text{g}$  per 1 mL of culture medium). After incubation for 24 h, the S protein reduced metabolic activity in all groups. However, there was only a significant reduction in HNEpC viability after the addition of the S protein at 2  $\mu\text{g}/\text{mL}$  (82.2%,  $p = 0.0006$ ; Figure 11A).

The DCF-DA assay showed that after incubation for 4 h with the S protein, intracellular ROS production was reduced (Figure 11B). A short detection time (5–10 min) did not reveal significantly reduced ROS levels. However, detection at 15 and 25 min revealed a reduction in ROS levels for 5 and 4  $\mu\text{g}/\text{mL}$  of the S protein, respectively. There were no differences for detection at 20 min.

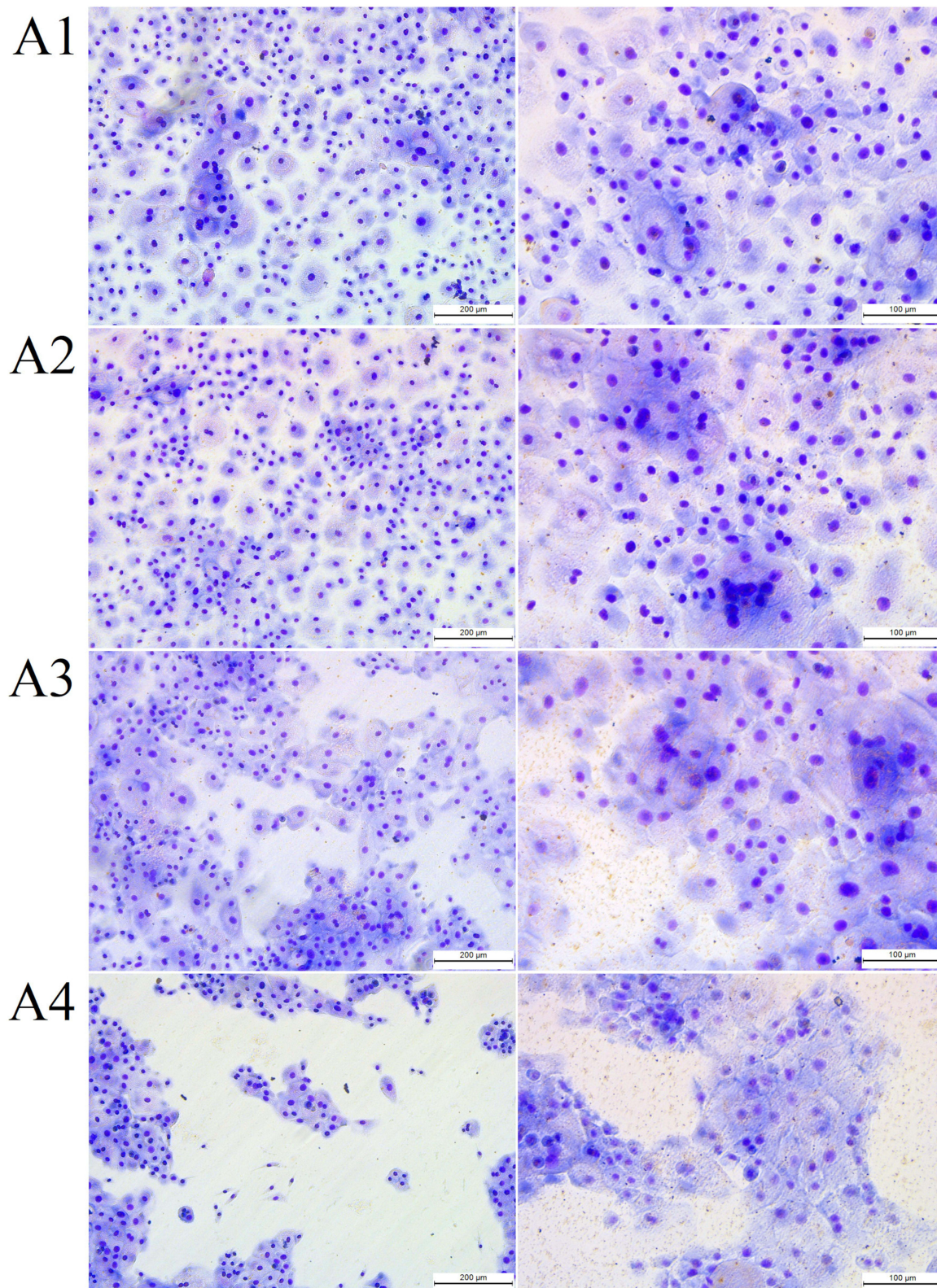


**Figure 5** The morphology of **(A1)** control primary human nasal epithelial cells (HNEpCs) and HNEpCs after the addition of **(A2)** 10, **(A3)** 50 and **(A4)** 100 mg/L fullereneol  $C_{60}(OH)_{40}$ . The cells were stained using May–Grunwald Giemsa method and visualised at two magnifications (the scale bar is 200  $\mu m$  on the left and 100  $\mu m$  on the right).

**Table 3** Quantitative Analysis of May–Grünwald Giemsa Morphological Images. In the Table, Asterisks Indicate the Level of Significance: (\*)  $p \leq 0.05$ , (\*\*)  $p \leq 0.01$

Research Group	Number of Cell Nuclei/mm <sup>2</sup>	SE	p-value	Area Covered by Cells (%)	SE	p-value
Control	394	26.0	<0.0001	58	9.7	0.0023
Fullerenol 10 mg/L	419	5.4		63	9.8	
Fullerenol 50 mg/L	302	43.3		63	12.1	
Fullerenol 100 mg/L	212**	76.3		54	16.4	
Ectoine 0.2%	488	49.8		64	10.9	
Ectoine 1%	455	9.0		56	11.2	
Ectoine 2%	499	26.5		54	16.1	
MIX low	369	20.6		62	12.5	
MIX medium	308	53.3		51	16.4	
MIX high	314	45.4		32*	7.4	

There were different results after incubation for 24 h with the S protein in the second assay (Figure 11C). In this case, we considered the reduced HNEpC viability after treatment with the S protein when calculating the ROS level. Intracellular ROS production was dependent on the S protein concentration; 2 µg/mL caused cellular oxidative stress. Similarly to the DCF-DA assay, the ROS level was reduced at an S protein concentration of 4 or 5 µg/mL, but the changes were not significant.

We also assessed ROS in the culture medium after incubation for 24 h with different S protein concentrations (Figure 11D). There were no significant differences, but there was a trend for an increase in ROS after adding the S protein at 2 µg/mL. For the subsequent experiments mimicking the adsorption of SARS-CoV-2 to the epithelium, we used an S protein concentration of 2 µg/mL because it produced the most pronounced increase in ROS production.

### The S Protein Had a Negative Charge, Agglomerated in Water and Had an Affinity for the Fullerenol–Ectoine Composite

TEM showed that the full-length recombinant S protein tended to clump into larger structures ranging in size from 75 to 120 nm. The observed particles were round and had an irregular, spike-like surface (Figure 12A). After mixing the S protein with the fullerenol–ectoine composite, we observed much smaller particles with a size of approximately several to several dozen nanometres around the protein (Figure 12B). Zetasizer measurements showed an average S protein size of  $96.7 \pm 16.8$  nm (Figure 12C) and an average zeta potential of  $-18.7 \pm 2.7$  mV.

### Fullerenol Reduced and Ectoine Increased the ACE2 Surface Area on HNEpCs

We evaluated the localisation of ACE2 on HNEpCs by using confocal microscopy. As shown in Figure 13, HNEpCs expressed ACE2 uniformly on their surface. Next, we added the S protein to each group except the negative control. Adding the S protein to HNEpCs increased ACE2 expression compared with the negative control (Figure 13B–E), regardless of the treatment group. We observed lower ACE2 expression in the fullerenol and MIX low groups compared with the positive control. The positive control and the ectoine groups had the strongest ACE2 expression. Morphologically, the surface of HNEpCs, and thus the ACE2 surface area, was largest after the addition of ectoine and the S protein.

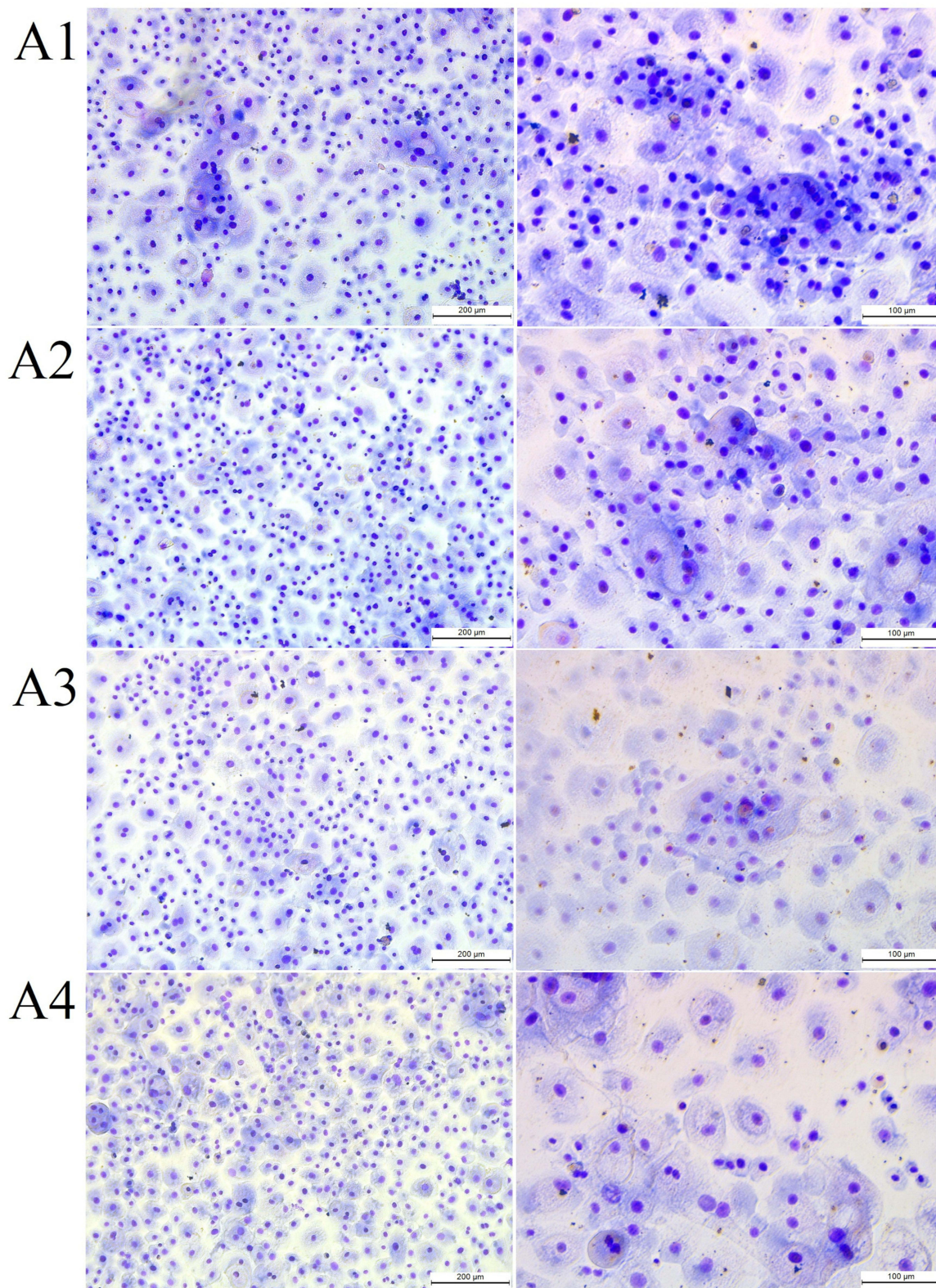


**Figure 6** The morphology of **(A1)** control primary human nasal epithelial cells (HNEpCs) and HNEpCs after incubation for 24 h with **(A2)** 0.2%, **(A3)** 1% and **(A4)** 2% ectoine. The cells were stained using the May–Grunwald Giemsa method and visualised at two magnifications (the scale bar is 200 μm on the left and 100 μm on the right).



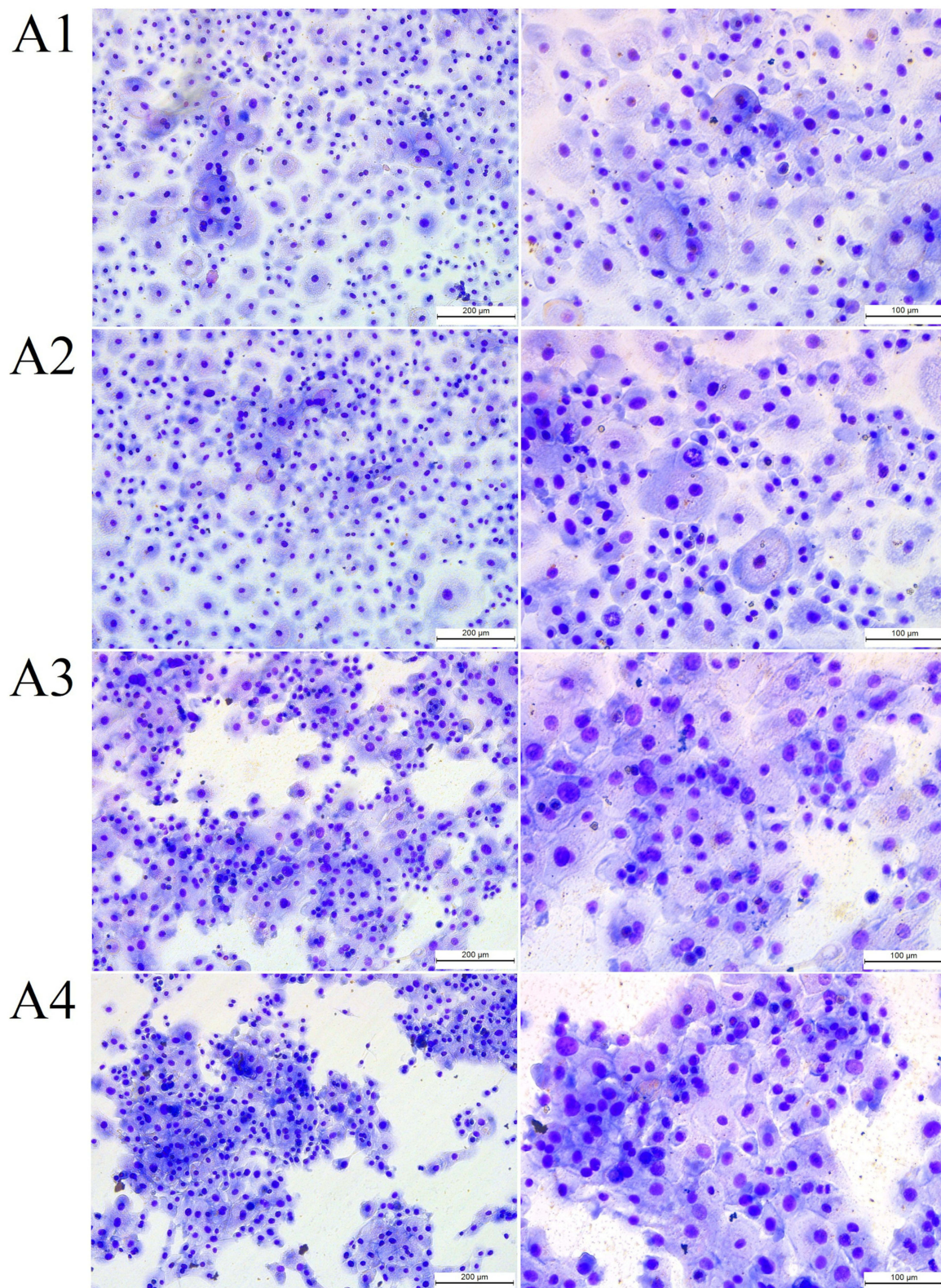


**Figure 7** The morphology of (A1) control primary human nasal epithelial cells (HNEpCs) and HNEpCs after incubation for 24 h with (A2) 0.2% ectoine and 10 mg/L fullerene (MIX low), (A3) 1% ectoine and 50 mg/L fullerene (MIX medium) and (A4) 2% ectoine and 100 mg/L fullerene (MIX high). The cells were stained using the May–Grunwald Giemsa method and visualised at two magnifications (the scale bar is 200  $\mu\text{m}$  on the left and 100  $\mu\text{m}$  on the right).

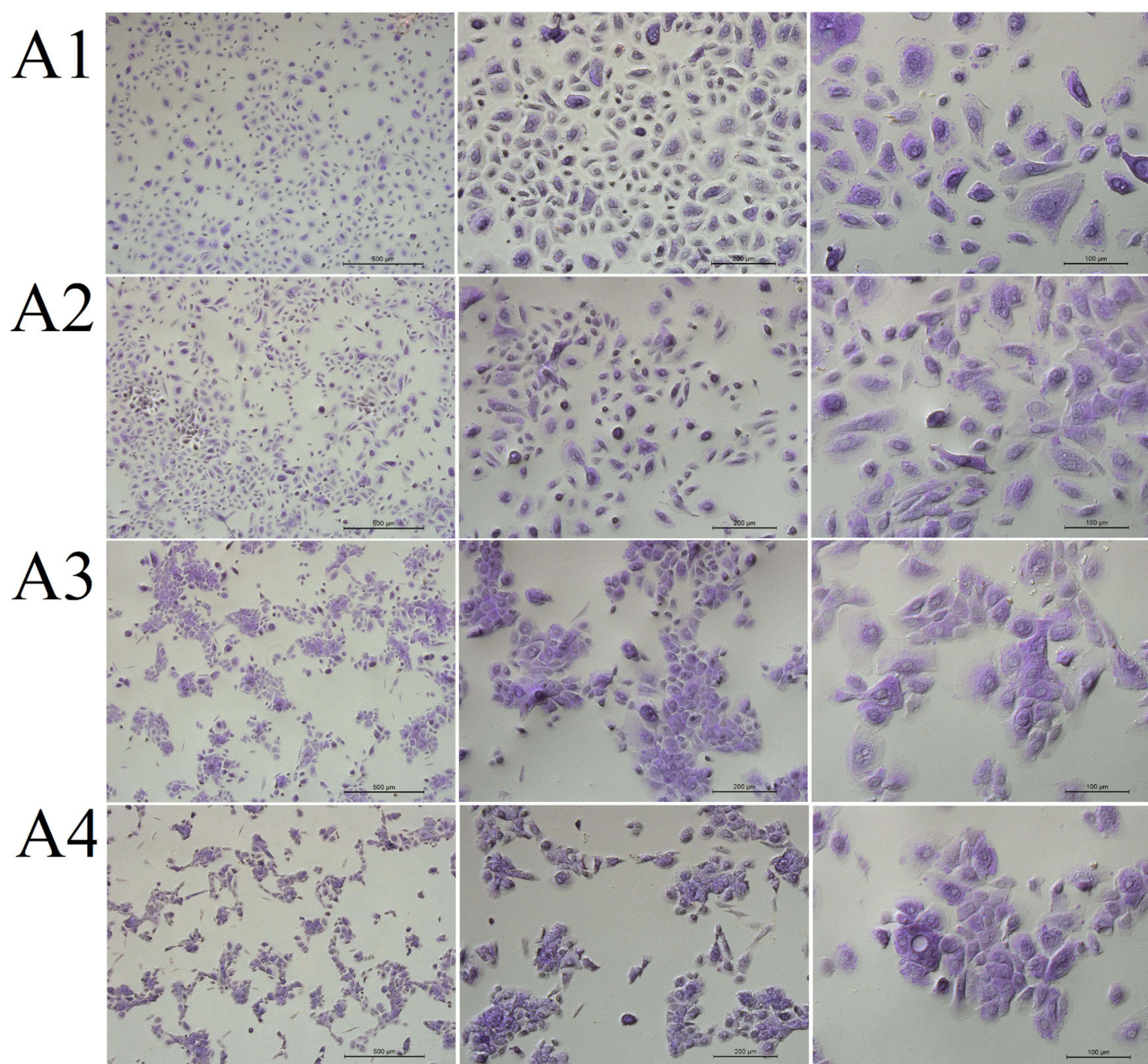


**Figure 8** The morphology of (A1) control primary human nasal epithelial cells (HNEpCs) and HNEpCs after incubation for 24 h with (A2) 10, (A3) 50 and (A4) 100 mg/L fullereneol  $C_{60}(OH)_{40}$ . The cells were stained with periodic acid–Schiff and haematoxylin and visualised at three magnifications (from left, the scale bar is 500, 200 and 100  $\mu\text{m}$ ).

## The Fullereneol–Ectoine Composite Protected HNEpCs Against the Cytokine Storm Caused by the S Protein

We analysed 40 cytokines involved in inflammatory processes (Figure 14). HNEpCs incubated with the active S protein for 24 h showed increased secretion of 24 of these cytokines into the culture medium, with a significant increase in interleukin 6 (IL-6), monocyte chemoattractant protein 1 (MCP-1), tissue inhibitor of metalloproteinases 2 (TIMP-2), macrophage colony-stimulating factor (M-CSF) and IL-8, and a trend for an increase in the expression of MCP-2 and eotaxin (Table 4). Pretreatment of HNEpCs with the fullereneol–ectoine for 1 h protected these cells from interaction with the S protein: these pretreated cells had cytokine levels that were similar to the control. There was only a tendency to increase the level of the M-CSF cytokine in the cell environment, which was statistically insignificant.

To exclude a potential inflammatory reaction of fullereneol itself, the study also compared the inflammatory profile of cells for individual components of the MIX-low composite. The results showed that, as we expected, the cytokine profile

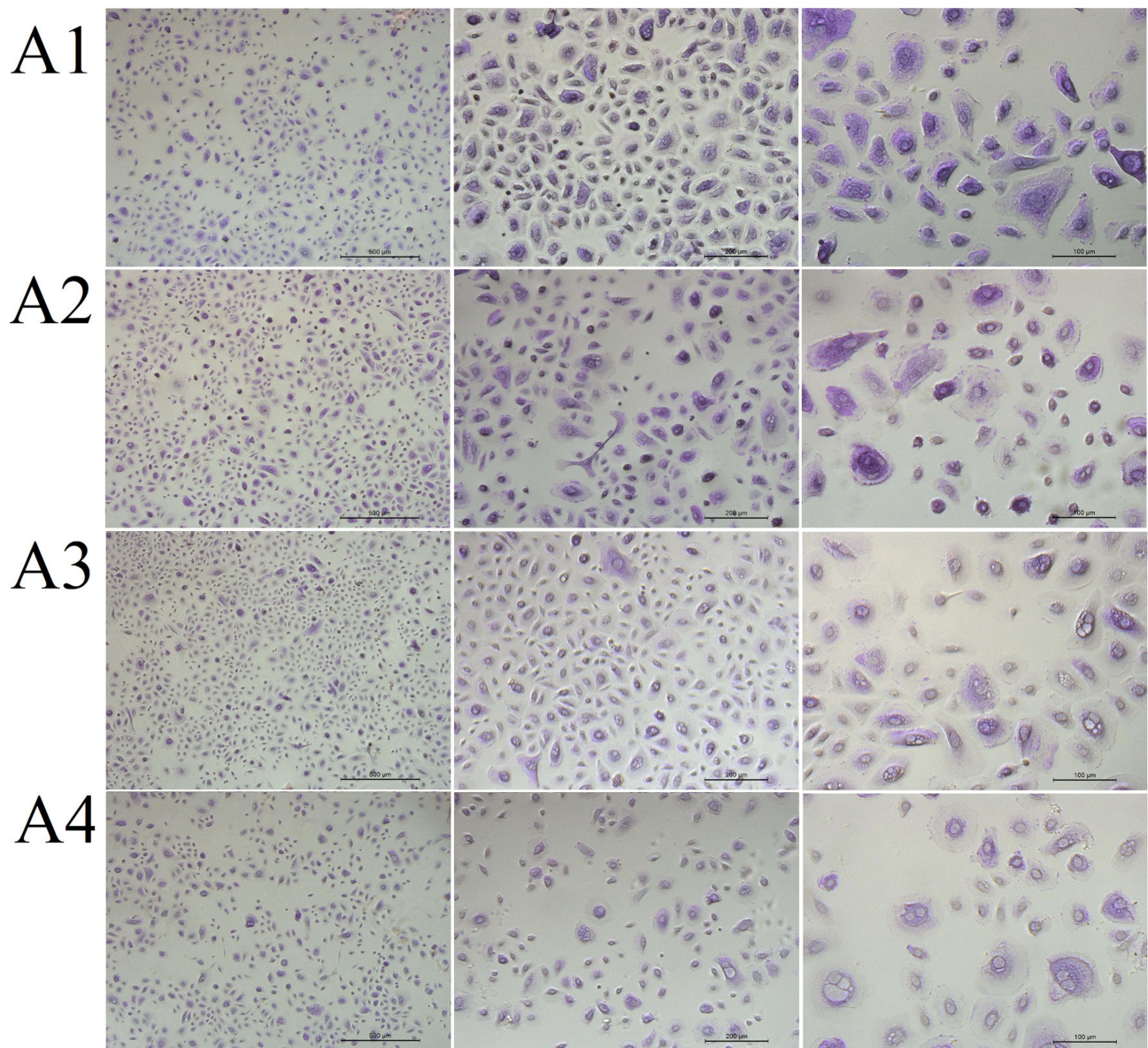


**Figure 9** The morphology of (A1) control primary human nasal epithelial cells (HNEpCs) and HNEpCs after incubation for 24 h with (A2) 0.2%, (A3) 1% and (A4) 2% ectoine. The cells were stained with periodic acid–Schiff and haematoxylin and visualised at three magnifications (from left, the scale bar is 500, 200 and 100  $\mu\text{m}$ ).

after the addition of fulleranol was similar to ectoine and even the level of some cytokines such as MCP-2, TIMP-2, IL-8 and granulocyte macrophage colony-stimulating factor (GM-CSF) was reduced. However, fulleranol increased the expression of IL-6 and MCP-1 compared to ectoine ([Figure S1](#)).

[Figure 15](#) shows the expression of genes encoding key proteins involved in viral envelope recognition and fusion with the host membrane (ACE2) and inflammation in HNEpCs. The addition of the S protein significantly increased the expression of ACE2 and key tested cytokines, such as IL-6 and TIMP2. However, the S protein did not significantly change MCP-1 and intercellular adhesion molecule (ICAM) expression and reduced IL-8 expression. The addition of the S protein to HNEpCs pretreated with the fulleranol–ectoine composite did not change ACE2 expression compared with the control. Furthermore, the expression of MCP-1, TIMP-2, ICAM and IL-8 was reduced after pretreatment of HNEpCs with the fulleranol–ectoine composite followed by S protein treatment compared with the control. IL-6 expression was significantly higher in the group pretreated with the fulleranol–ectoine composite and then treated with the S protein compared with the control group and was comparable to the group treated with only the S protein.

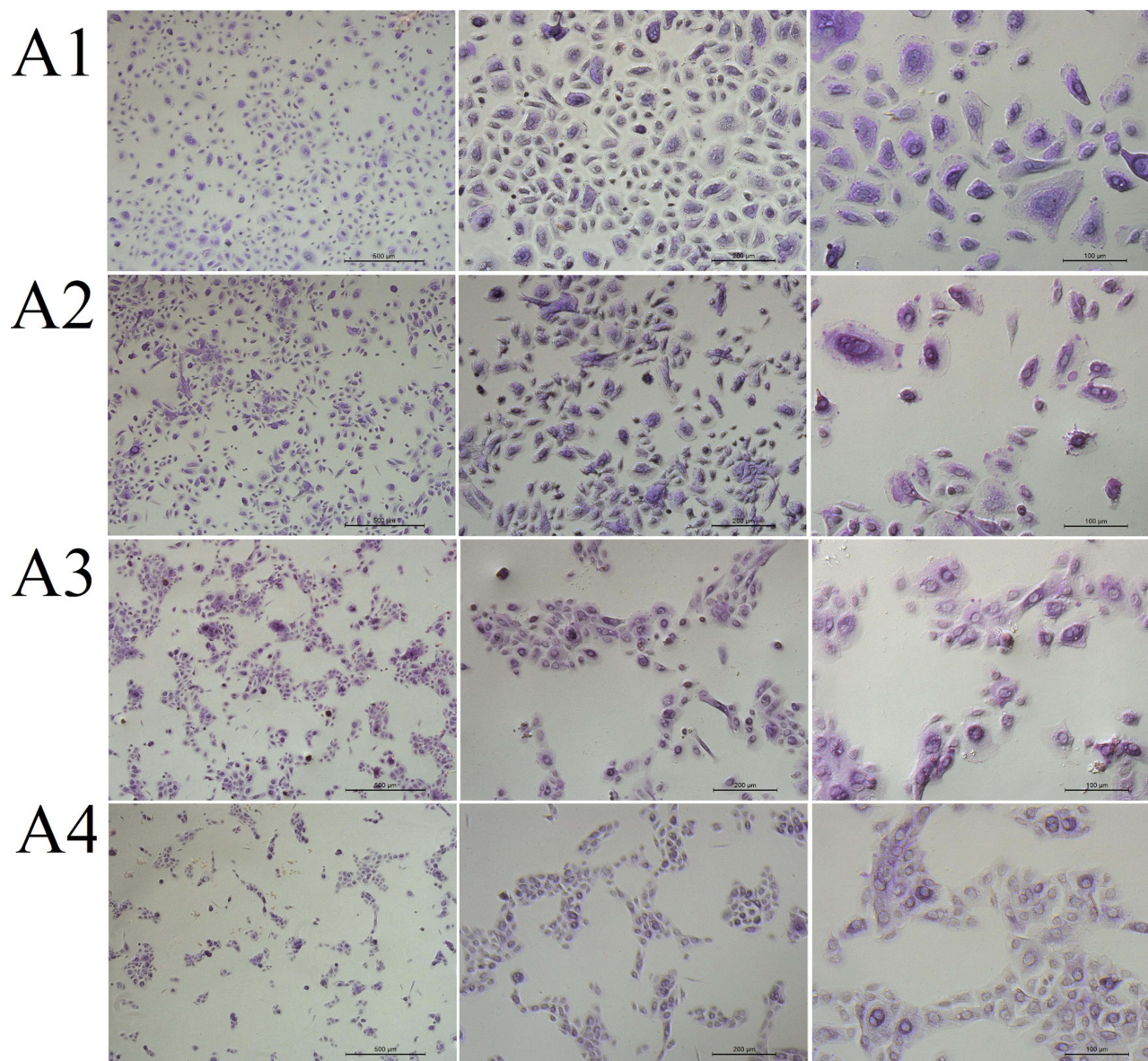


**Figure 10** The morphology of **(A1)** control primary human nasal epithelial cells (HNEpCs) and HNEpCs after incubation for 24 h with **(A2)** 0.2% ectoine and 10 mg/L fullereneol (MIX low), **(A3)** 1% ectoine and 50 mg/L fullereneol (MIX medium) and **(A4)** 2% ectoine and 100 mg/L fullereneol (MIX high). The cells were stained with periodic acid–Schiff and haematoxylin and visualised at three magnifications (from left, the scale bar is 500, 200 and 100  $\mu\text{m}$ ).

## Discussion

The main target of SARS-CoV-2 is respiratory epithelial cells. Therefore, we decided to perform our experiments using HNEpCs derived from human nasal mucosa; they represent a coculture of ACE2-expressing cells such as sustentacular cells, microvillous cells, Bowman's gland cells, basal cells and pericytes.<sup>4</sup> Respiratory viruses lead to dysfunctional secretion of cytokines, ions and mucus and increased adenosine triphosphate (ATP) levels.<sup>21</sup> COVID-19 is accompanied by two main clinical phases: viral infection of target cells and the cytokine storm.<sup>22</sup> Our study comprised three steps. First, we performed physicochemical characterisation of fullereneol, ectoine and their composite and assessed their toxicity towards HNEpCs. Second, we determined the impact of the SARS-CoV-2 S protein on the viability, ROS production and inflammatory cytokine profile of HNEpCs. Finally, we evaluated the ability of the fullereneol–ectoine composite to act as a coating to protect cells from the S protein. We have submitted a patent for our novel device (Poland patent, P.448505).<sup>23</sup> According to standard 10993 developed by the International Organization for Standardization,

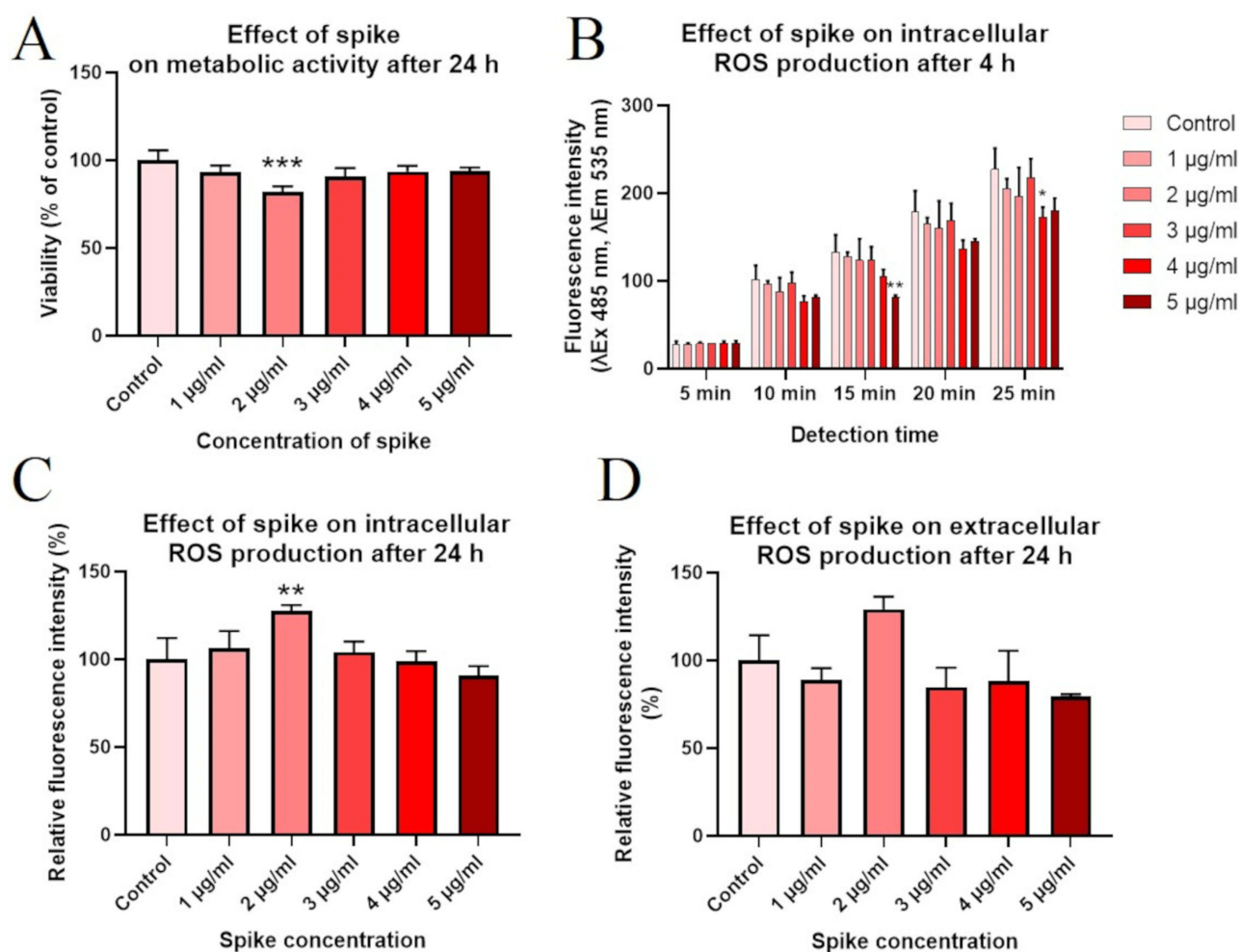


**Figure 11** The effect of different concentrations of the spike (S) protein from severe acute respiratory syndrome coronavirus 2 (SARS-CoV-2) on (A) primary human nasal epithelial cell (HNEpC) viability, the intracellular reactive oxygen species (ROS) content after incubation for (B) 4 and (C) 24 h, and (D) the extracellular ROS content after incubation for 24 h. In the figure, asterisks indicate the level of significance: (\*)  $p \leq 0.05$ ; (\*\*)  $p \leq 0.01$  and (\*\*\*)  $p \leq 0.001$ .

a potential medical device should protect cells against viruses mechanically, without pharmacological, immunological or metabolic effects. In particular, nasal epithelial cells constitute the first protective barrier against damage, foreign bodies and infections and have secretory and transport functions.<sup>24</sup> To strengthen the effect of this natural protective barrier, we designed a platform consisting of ectoine, which does not penetrate cell membranes, functionalised with fullerene with previously proven anti-inflammatory and antioxidant properties.<sup>25</sup>

According to Schramm et al,<sup>24</sup> the cells most sensitive to the action of the fullerene family (including carbon nanotubes) are nasal epithelial cells, followed by the cells of the alveoli; bronchial epithelial cells are the least sensitive. HNEpCs showed approximately 55% metabolic activity after incubation for 24 h with 100 mg/L carbon nanotubes. In contrast to that study, we demonstrated that fullerene, as another allotrope of carbon, was safe and did not cause cytopathic effects on HNEpCs at a concentration of 10, 50 and 100 mg/L after incubation for 24 h. However, its toxicity increased at a longer exposure time (48 h). Ershova et al<sup>26</sup> reported similar observations: a C<sub>60</sub> fullerene derivative containing 3-phenylpropionic acid and a chlorine atom did not affect the viability of human primary lung fibroblasts (HELFs) after a short exposure time (3 h), likely because fullerene did not manage to enter the cytoplasm. Wang et al<sup>27</sup> found that the incubation of human lung adenocarcinoma cells with C<sub>60</sub> fullerene at a concentration of up to 200 µg/mL for 7 h did not affect the metabolic activity of the cells. It seems that the toxicity of fullerenes associated with long exposure times (>24 h) is conditioned by their ability to penetrate the cell and enter the cytoplasm due to their lipophilic nature. The concentration of fullerenes is also important: according to Ershova et al,<sup>26</sup> a concentration of >0.1 µM slowed

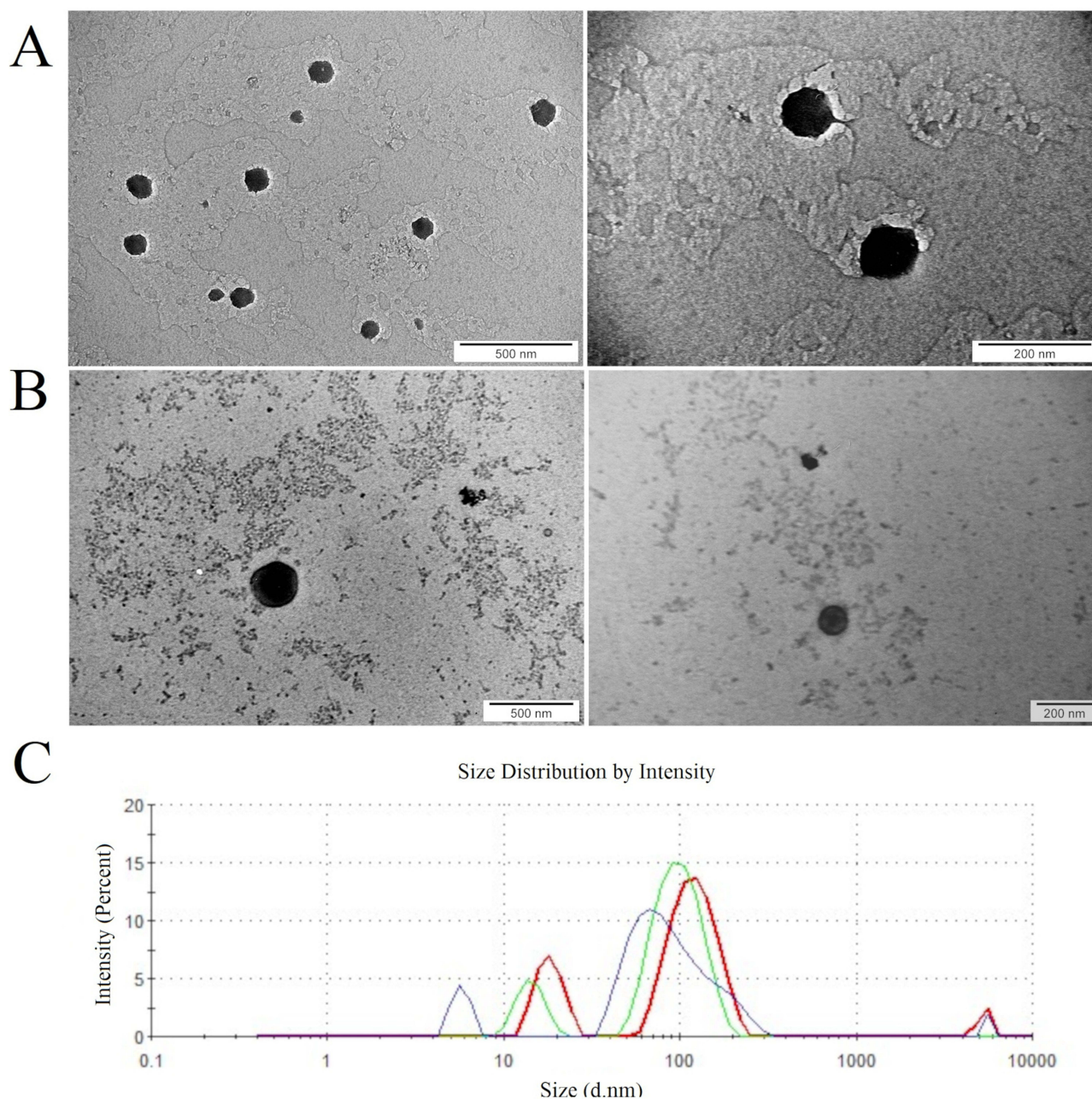


**Figure 12** (A) The morphology of the spike (S) protein from severe acute respiratory syndrome coronavirus 2 (SARS-CoV-2) and (B) the interaction between the S protein and the fullerene-ectoine composite observed under a transmission electron microscope. The scale bar is 500 and 200 nm, respectively. (C) The size distribution of the S protein after suspension in water, measured using a Zetasizer.

down the proliferation of HELFs, and a low nanomolar concentration increased 3-[4,5-dimethylthiazol-2-yl]-2,5-diphenyltetrazolium bromide reduction, leading to higher viability.<sup>26</sup> Reduced HNEpC viability may be associated with reduced expression of cell cycle markers, including Ki-67 and proliferating cell nuclear antigen, and an increase in ROS production and DNA strand breaks.<sup>26</sup> Sayers et al<sup>11</sup> showed that fullerenes inhaled by mice and rats for 13 weeks at a concentration of 2 mg/m<sup>3</sup> did not affect the systemic immune function but caused inflammatory reactions in the lungs. The toxicity of fullerenes is also influenced by their surface chemistry. According to Chen et al,<sup>28</sup> polyhydroxylated C<sub>60</sub> (OH)<sub>7±2</sub> fullerenes, regardless of the dose, protected isolated perfused lungs and RWA 264.7 murine macrophages against oxidative stress induced by sodium nitroprusside and hydrogen peroxide. Moreover, the uptake and cytotoxicity of fullereneols depend on the cell line and the serum content of the medium. In one study, the lethal concentration LC50 for

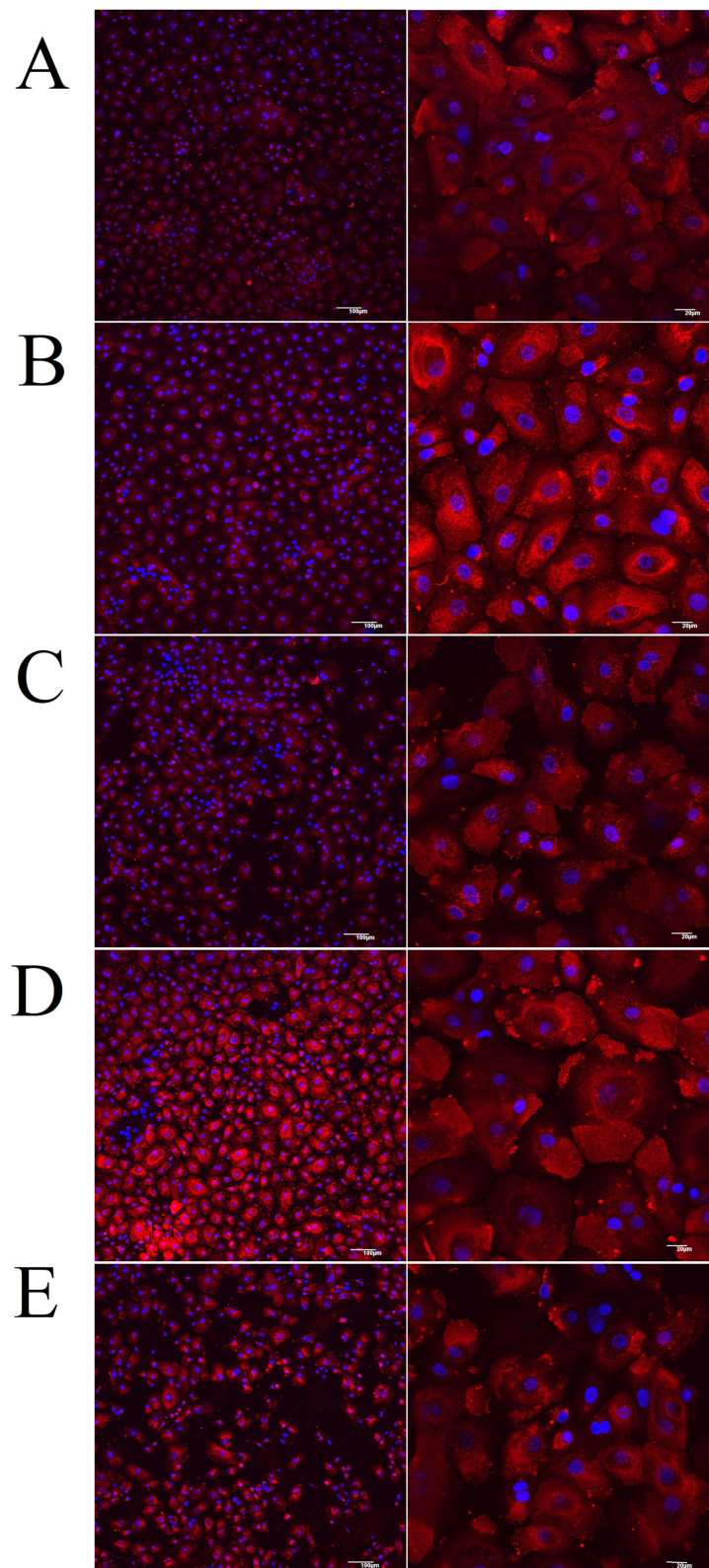


**Figure 13** The presence of angiotensin-converting enzyme 2 (ACE2) on the surface of (A) control primary human nasal epithelial cells (HNEpCs) and HNEpCs incubated for 24 h with (B) the spike (S) protein, (C) fulleranol and the S protein, (D) ectoine and the S protein and (E) 0.2% ectoine and 10 mg/L fulleranol (MIX low) and the S protein. ACE2 immunofluorescence is shown in red. Blue staining shows cell nuclei stained with 4',6-diamidino-2-phenylindole (DAPI). The scale bar is 100 μm (left side) and 20 μm (right side).

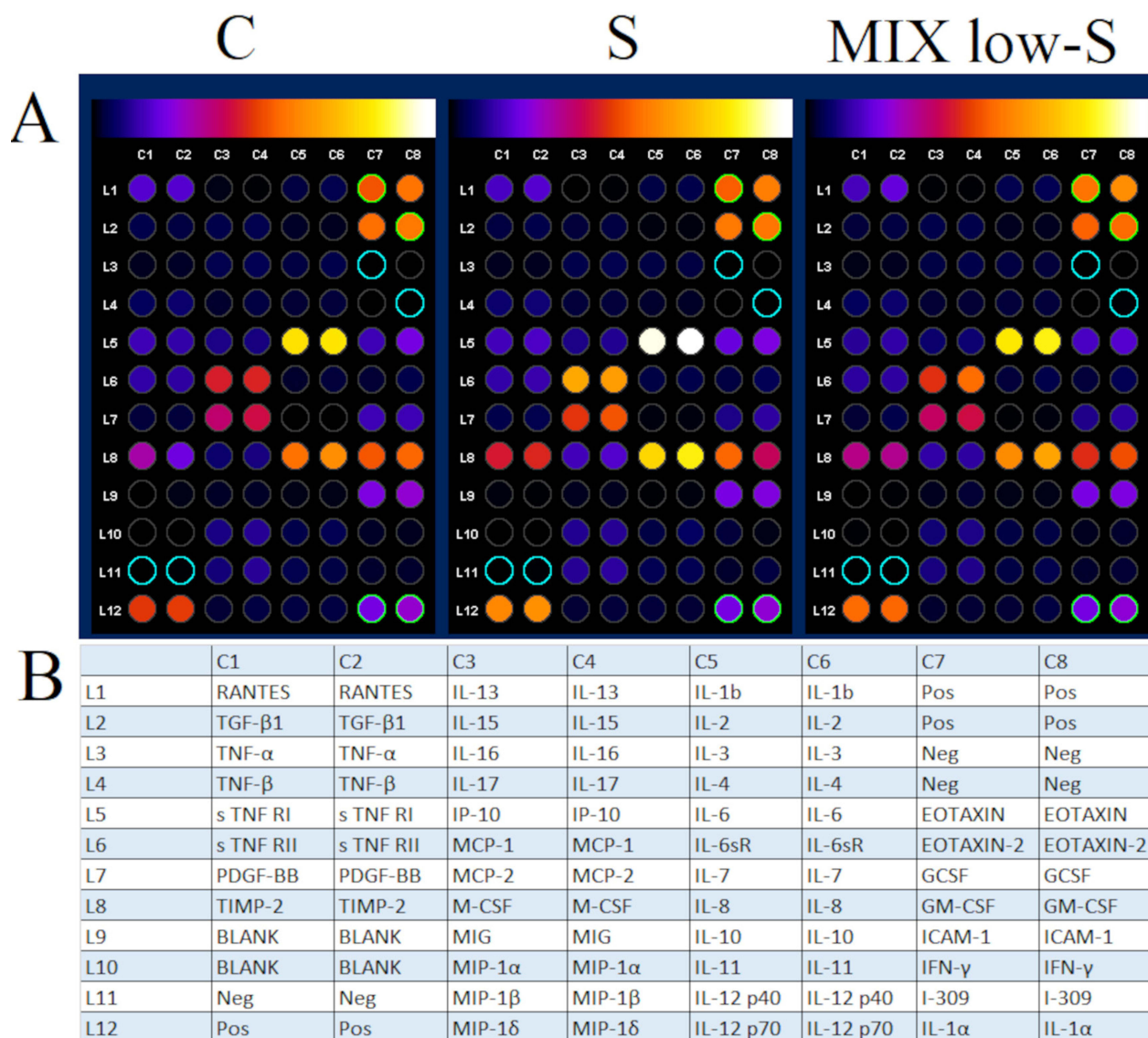


**Figure 14 (A)** Analysis of cytokines secreted into the culture medium by control primary human nasal epithelial cells (HNEpCs), by HNEpCs incubated for 24 h with the spike (S) and by HNEpCs pretreated for 1 h with 0.2% ectoine and 10 mg/L fullereneol (MIX low) and then incubated for 24 h with the S protein. The results were normalised to control dots and background (blanks) were subtracted in ImageJ 1.54d. **(B)** The table shows the list of proteins found on the array.

**Abbreviations:** RANTES, regulated upon activation; normal T cell expressed; and secreted; IL, interleukin; Pos, positive control; TGF-β1, transforming growth factor β1; TNF, tumour necrosis factor; Neg, negative control; sTNFR, soluble tumour necrosis factor receptor; IP-10, interferon-inducible protein-10; MCP, monocyte chemoattractant protein; PDGF, platelet-derived growth factor; GCSF, granulocyte-colony stimulating factor; TIMP, tissue inhibitor of metalloproteinases; M-CSF, macrophage colony-stimulating factor; GM-CSF, granulocyte macrophage colony-stimulating factor; MIG, monokine induced by interferon-γ; ICAM-1, intercellular adhesion molecule 1; MIP, macrophage inflammatory protein; IFN-γ, interferon γ; I-309, small-inducible cytokine A1.

Chinese hamster ovary cells, Chinese hamster lung cells and L929 cells (a mouse fibroblast line) was 199, 75 and 1000 g/mL respectively. Moreover, fullereneol in the presence of serum is more difficult to penetrate cell membranes.<sup>29</sup> In other studies, C<sub>60</sub>(OH)<sub>n</sub>(n: 18–22) at a concentration of 1600 μg/mL slightly inhibited the viability of healthy human IMR-90 lung cells (23%), while at a concentration of 25 μg/mL, it was completely non-toxic.<sup>30</sup>

Ectoine is a commonly used protective agent against environmental stresses such as heat, radiation and high salinity. We and Rieckmann et al<sup>31</sup> demonstrated a strong relationship between the ectoine concentration and cytotoxicity. Rieckmann et al<sup>31</sup> showed that 70 and 140 mM ectoine, corresponding to 1% and 2%, was cytotoxic to head and neck squamous cell carcinoma (HNSCC) cells and reduced the proliferation of primary fibroblast cells (F184; NHF) to a lesser



**Table 4** Relative Interleukin 6 (IL-6), Monocyte Chemotactic Protein 1 (MCP-1), Monocyte Chemotactic Protein 2 (MCP-2), Tissue Inhibitor of Metalloproteinases 2 (TIMP-2), Macrophage Colony-Stimulating Factor (M-CSF), Interleukin 8 (IL-8) and Eotaxin Protein Levels

Protein	Research Group ANOVA			ANOVA	
	Control	Spike Protein	Fullerenol-Ectoine Composite and Spike Protein	Standard Error	p-value
IL-6	100	121.19*	102.06	5.598	0.0088
MCP-1	100	153.06*	116.16	9.549	0.0209
MCP-2	100	127.20	101.07	7.133	0.0611
TIMP-2	100	173.40*	131.34	8.769	0.0327
M-CSF	100	190.37*	148.64	2.491	0.012
IL-8	100	135.87*	108.28	9.242	0.0227
Eotaxin	100	117.58	91.21	7.912	0.437

**Note:** In the Table, Asterisks Indicate the Level of Significance: (\*)  $p \leq 0.05$ .

extent after 3 days. However, 4% ectoine reduced the number of HNSCC cells to zero. We found that 2% ectoine reduced HNEpC viability by 30%, while incubation with 0.2% and 1% ectoine for 24 h did not affect HNEpC viability. However, incubation for 48 h reduced HNEpC viability by 20% regardless of the ectoine concentration. Yao et al<sup>32</sup> reported similar results: 80% viability of mouse B16-F0 cells and human melanoma A2058 cells after treatment with 500  $\mu$ M ectoine 3 days.<sup>32</sup> The cytotoxic effect of ectoine appears to be complex and depends on the cell line, exposure time and concentration. Ectoine is an osmolyte and in an environment with normal salt concentrations, it may cause oxidative stress similar to the effect of NaCl. Moreover, high ectoine concentrations can also inhibit protein functions, as reported previously for tyrosinase.<sup>32</sup>

The available studies that have combined ectoine and carbon nanomaterials have only focused on the impact of carbon materials on ectoine production,<sup>33</sup> as well as the protective effect of ectoine against carbon nanomaterials inhaled into the lungs, which in the long term cause fibrosis and cancer of lung.<sup>34</sup> Fatollahi et al<sup>33</sup> showed that multi-walled carbon nanotubes at a concentration of 100 mg/L increased the production of ectoine by *H. elongata* by 67%. Moreover, carbon nanoparticles increased cytokines, proliferation and apoptosis in vitro and in vivo, and this effect was inhibited by 1 mm ectoine.<sup>34</sup> Thus, inhalation of carbon nanoparticles into the lungs has long been associated with adverse health effects in the respiratory tract. Our study is the first to evaluate a mixture containing ectoine and fullereneol C<sub>60</sub>(OH)<sub>40</sub>. When incubated for 24 h, it was fully biocompatible with HNEpCs and caused only a 25% decrease in cell viability after 48 h. It is worth noting that 2% ectoine alone exerted cytotoxicity after incubation for 24 h; however, this effect was reversed by combining it with 100 mg/L fullereneol. According to ISO 10993 Biological Evaluation of Medical Devices – Part 5: Tests for in vitro cytotoxicity, reduction of cell viability by more than 30% is considered a cytotoxic effect in XTT assay. In both cases, the composite was therefore biocompatible.

The physicochemical properties of fullereneol differ from carbon pollutants inhaled through the lungs. One C<sub>60</sub> fullerene particle always contains 30 double bonds, which are responsible for the reactivity of the structure. Two substituents in the fullereneol structure use one carbon double bond,<sup>28</sup> so the C<sub>60</sub>(OH)<sub>40</sub> structure is much less reactive than C<sub>60</sub> and, thus, much less toxic. Fullereneol has numerous physicochemical properties that may be useful in protection against viral antigens, such as electronegativity, ease of functionalisation, good solubility in water and a well-defined shape and size. As we have shown in this work, both fullereneol and ectoine have a negative charge similar to the S protein. Therefore, we speculate that fullerenes can block the active sites of membrane receptors, as shown previously for human immunodeficiency virus 1 protease.<sup>35</sup> Moreover, the size and shape of fullereneol can mimic the circular 97-nm SARS-CoV-2 spike particles and therefore occupy their active sites. In addition, fullerene and its derivatives can generate

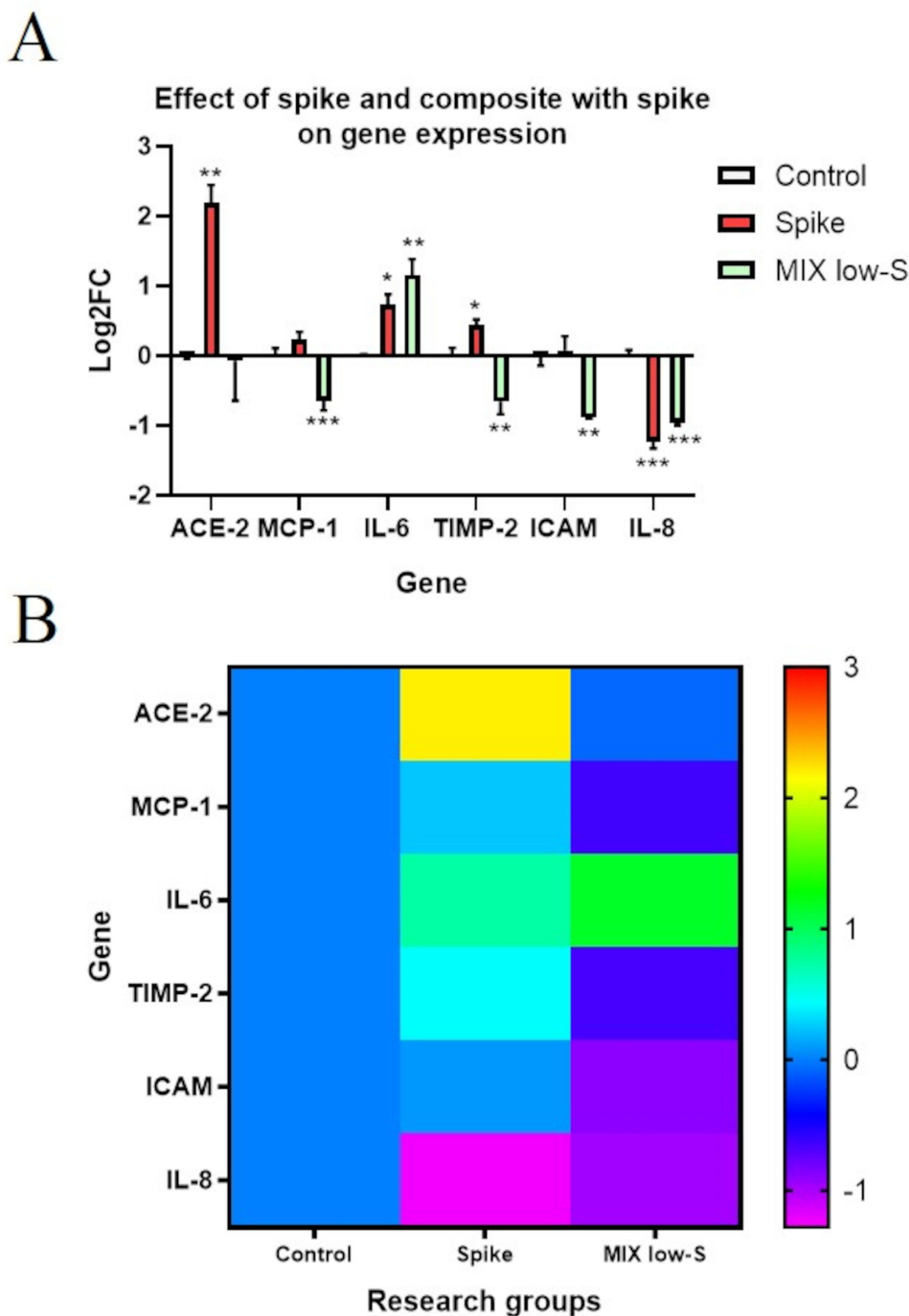


**Figure 15** Analysis of angiotensin-converting enzyme 2 (ACE2), monocyte chemoattractant protein 1 (MCP-1), interleukin 6 (IL-6), tissue inhibitor of metalloproteinases 2 (TIMP-2), intercellular adhesion molecule (ICAM) and IL-8 gene expression in the control primary human nasal epithelial cells (HNEpCs), in HNEpCs after incubation for 24 h with the S (spike) protein, and in HNEpCs pretreated for 1 h with 0.2% ectoine and 10 mg/L fullereneol and then incubation for 24 h with the S protein (MIX low-S). The results are presented as log<sub>2</sub> fold-change (FC) in the form of (A) a bar chart with standard deviation and (B) a heat map. Values above/below 0 indicate upregulation/downregulation of gene expression. Relative expression was calculated using the GAPDH gene expression and the control group (0). In the figure, asterisks indicate the level of significance: (\*) p ≤ 0.05; (\*\*) p ≤ 0.01 and (\*\*\*) p ≤ 0.001.

singlet oxygen when illuminated even in the visible light range (535 nm), which damages the protein structures of the virus envelope and cannot be controlled during experiments.<sup>36</sup>

In this work, we used a composite of fullereneol and ectoine for the first time, and we wanted to check whether there were any interactions between them. According to our UV–Vis studies and other authors, the aqueous solution of fullerene is

characterized by peaks at 208, 265 and 347 nm.<sup>37</sup> It is known that the UV spectrum of ectoine shows strong absorbance at about 210 nm and still absorbs light at about 365 nm.<sup>38</sup> Mixing of ectoine and fullereneol caused a small shift of the peak at 225 nm by 1 nm, which is likely the consequence of the formation of the non-covalent complex. As previously reported by Butowska et al<sup>39</sup> fullereneol can interact with other molecules, such as doxorubicin, via delocalized  $\pi$  electrons of the  $C_{60}$  cage. In addition, ectoine has a proven affinity for negatively charged phosphate backbones in DNA. It seems that ectoine can also interact with fullerene, especially in the environment of water, when ectoine binds with seven water molecules and thus forms an ectoine-water complex in the environment of bioparticles.<sup>38</sup> Another important feature of the UV–Vis spectrum of the fullereneol and ectoine composite was the increase in absorbance in the whole range of wavelengths studied upon the addition of ectoine. As reported by Prylutskyy et al,<sup>37</sup> this is a common property of fullerene solutions, which is typically associated with additional light scattering due to ligand-induced additional aggregation of fullerene. The UV–Vis spectrum of the composite resembled that of ectoine due to the high weight content of this osmolyte in the mixture. Additionally, we showed that the stability of fullereneol (based on the zeta potential) increased after the addition of ectoine. Specifically, the particles  $C_{60}(OH)_{40}$  repel each other more strongly and their average size is smaller.

HNEpCs are epithelial cells that form tight intercellular connections. However, as a result of chronic rhinitis, epithelial–mesenchymal transformation (EMT) occurs – that is, the loss of expression of markers responsible for the epithelial phenotype and the acquisition of migratory, mesenchymal cell characteristics. This remodelling of nasal tissue leads to the formation of polyps and difficulty breathing.<sup>40</sup> In our work, we observed tight cell–cell connections after the addition of fullereneol and the fullereneol–ectoine composite at high concentrations. This is the first evidence that the materials used – in particular, fullerene derivatives – can inhibit inflammation and EMT, as shown previously in liver cancer cells, and affect the tightness of the protective barrier. Castro-Ochoa et al<sup>41</sup> demonstrated that ectoine reduced epithelial permeability and protected the architecture of epithelial junctions during colitis as a result of maintaining the expression of key tight junction proteins (occludin and zonula occludens-1) and reducing the expression of inflammatory cytokines (interferon- $\gamma$ , tumour necrosis factor  $\alpha$  [TNF $\alpha$ ], keratinocyte chemoattractant and IL-1 $\beta$ ).

The nasal mucosa is the first barrier protecting against the entry of pathogens into the lower respiratory system. Mucolytic enzymes secreted by bacteria and cytolytic viruses destroy the continuity of the mucosa, which promotes subsequent infections on the nasal epithelium.<sup>42</sup> The mucus on the mucous membrane, consisting mainly of mucins, is responsible for the selective control of the transport of pollutants and viruses. Mucins interact with other mucins and mucus components, including lipids, immunoglobulins, salts and cellular debris, via electrostatic interactions, hydrophobic interactions, hydrogen bonds and/or disulfide bonds.<sup>42</sup> In this way, a viscoelastic layer of mucus is formed on the mucosal surface, which makes it difficult for the virus to anchor.<sup>9</sup> On the other hand, excessive secretion of mucins accompanies many pathological conditions related to inflammation, including asthma and cystic fibrosis.<sup>43</sup> In our study, fullereneol and ectoine did not affect PAS staining, which detects glycogen, sulfomucins, epithelial sialomucins and neutral mucosal substances. In the case of ongoing inflammation, ILs induce mucus secretion and there is an increased proportion of goblet cells in the co-culture; these cells have a dark purple colour.<sup>44</sup> Our study provides the first evidence that the tested materials are not pro-inflammatory.

The full-length S protein, or even its S1 subunit or the RBD, alone without other viral components can induce changes in the signalling of pulmonary artery smooth muscle cells, pulmonary artery endothelium and muscle cells.<sup>3,45</sup> In those studies, the authors used antigen at concentrations of 5 or 10  $\mu\text{g}/\text{mL}$ .<sup>3,45</sup> We used several S protein concentrations – 1, 2, 3, 4 and 5  $\text{ng}/\text{mL}$  – and observed concentration-dependent cytotoxicity to HNEpCs. Interestingly, we observed a mild cytotoxic effect after adding 2  $\mu\text{g}/\text{mL}$  of the S protein; the other concentrations did not reduce the metabolic activity of cells. This effect could be related to agglomeration of the S protein at high concentrations. In previous studies, researchers have reported no effect of the S protein subunits on the viability of human brain microvascular endothelial cells, human bronchial epithelial cells (the BEAS-2B cell line), lung cancer cells and microglia (the HMC3 cell line).<sup>46,47</sup> However, the sustained metabolic activity of cells after addition of the S protein does not exclude its effect on the loss of epithelial electrical resistance,<sup>46,48</sup> promoting inflammation and inducing metalloproteinases.<sup>46</sup> Long exposure to the S protein (>72 h) would likely increase the rate of cell death as occurs in severe cases of COVID-19, where oxidative stress and the cytokine storm promote cytotoxicity. Keturakis et al<sup>49</sup> noticed a relationship between the action of the RBD epitope of the S protein under normal and hypoxic conditions. The induction of damage to rat cardiomyocytes was associated with impaired mitochondrial activity, but under hypoxic conditions. Therefore, in addition to the tight epithelium, the cell microenvironment may

also determine the sensitivity of cells to infection. In one study, the S1 protein exerted a much greater systemic toxicity *in vivo* after intravenous injection of 35 µg into transgenic mice carrying human ACE2 than the toxicity observed *in vitro*. Specifically, exposure to the S1 protein for 3 days induced lung damage and fibrosis, the recruitment of inflammatory cells, endothelial cell dysfunction and the formation of thrombi and emboli in pulmonary vessels.<sup>50</sup>

Oxidative stress is associated with acute respiratory failure and airway epithelial damage<sup>51</sup> as a result of contact of SARS-CoV-2 or the S protein with ACE2, which stimulates ROS production by activating NADPH oxidases (NOXs). The main mediator of inflammation, IL-6, is involved in the upregulation of NOXs in cells.<sup>51</sup> Oxidative stress can develop in the respiratory epithelium and its surroundings, namely the endothelium of pulmonary vessels.<sup>51</sup> Consistent with previous studies, we found that even the S protein itself increased intracellular ROS levels 24 h after its addition. Oxidative stress under the influence of the S protein has been reported previously.<sup>51–53</sup> The S protein induces inflammation by increasing intracellular ROS levels and inhibiting the phosphatidylinositol 3-kinase (PI3K)/AKT/mammalian target of rapamycin (mTOR) signalling in bronchial epithelial and vascular endothelial cells.<sup>53</sup> In that study, the authors found that both the virus and the S protein caused apoptosis, suggesting a key role of the S protein–ACE2 connection in the survival of respiratory epithelial cells. In another study, the S protein induced senescence in ARPE-19 retinal pigmented epithelium cells by upregulating the ROS/p53/p21 pathway.<sup>52</sup> Thus, as a result of contact with the viral envelope and ROS production, the nasal epithelium ages faster and loses its protective functions due to loss of integrity.

The S protein also increased intestinal ROS in the Caco-2 model; the authors proposed a mechanism related to diarrhoea during infection. These authors showed a rapid increase in intestinal ROS with a peak ROS within 15 min after spike exposure and 30 min of incubation with DCF-DA.<sup>54</sup> In our work, 4-hour spike exposure caused a decrease in ROS levels and this effect was dependent on the detection time of DCF-DA and spike concentration. A decrease in ROS was observed after 15 and 25 min for 5 and 4 µg/mL protein S, respectively. Since spike is an oxidative protein, the reduced ROS level could be due to an imbalance between ROS production and antioxidant systems.<sup>54</sup> Jiang et al explained that excessive production of oxygen radicals triggers the antioxidant defense systems of the cell, which may be the cause of the decrease in ROS with exposure time.<sup>55</sup> Oxygen radicals naturally occur in cells, which are signaling molecules and can be regulated at the cellular level, specific to a given tissue.<sup>56</sup> In addition, DCF-DA acts on the principle of passive diffusion into cells and is oxidized to a fluorescent form inside the cells. It seems that even small time differences in the addition of DCF-DA can have a significant effect on the obtained signal. After 20 min of DCF-DA addition, the ROS level in cells, regardless of spike concentration, was similar to the control as previously described by other authors for 60 min.<sup>57</sup> Poeta et al<sup>57</sup> reported that after adding thermally inactivated SARS-CoV-2 (1 µg/mL) and spike (1 µg/mL) to Caco-2 cells, an initial 2.5–3-fold increase in ROS was observed, and after 60 min, the level returned to the control level. The authors of this work demonstrated that the normalization of ROS levels after an hour was independent of intestinal cell viability and apoptosis,<sup>57</sup> so it could have resulted from the action of the spike as a redox modulator as well as antioxidant defense systems such as superoxide dismutase for O<sup>2•</sup> or peroxidase for H<sub>2</sub>O<sub>2</sub>.<sup>56</sup> It should also be remembered that ROS has a millisecond lifespan and their levels change rapidly, which results from the rate of generation, chemical reactions and diffusion. In addition, fluorescent probes for measuring ROS are sensitive to oxygen and pH, which is associated with the nonlinearity of their amount over time.<sup>56</sup>

We found that the S protein increased ACE2 expression on the surface of HNEpCs, similarly to what was reported for the BEAS-2B cell line;<sup>58</sup> this change may facilitate virus entry into cells. ACE2 expression determines the efficiency of coronavirus infection of host cells; upregulation of this protein by the S protein facilitates invasion. For this reason, messenger RNA (mRNA)-based vaccines encoding the S protein may carry some danger due to long-term overexpression of ACE2.<sup>58</sup> On the one hand, the S protein can promote viral invasion and, on the other hand, promote cell humoral immunity. We used the S protein to mimic natural viral infection.

Hyper-inflammation caused by SARS-CoV-2 is a life-threatening condition and causes pulmonary oedema, impaired oxygen exchange and acute respiratory distress syndrome.<sup>59</sup> SARS-CoV-2 infection is associated with increased expression of cytokines, including IL-13, MCP-1 and interferon  $\gamma$ -induced protein (IP-10), in patients with sepsis.<sup>60</sup> Because SARS-CoV-2 infection increases inflammation, we evaluated whether the S protein could cause a similar effect. We clearly showed that 2 µg/mL of the full-length S protein (1211 amino acids) increased the level of most of the tested cytokines in the HNEpC culture medium, in particular IL-6, MCP-1, TIMP-2, M-CSF and IL-8. We also noted elevated IL-6 and TIMP-2 mRNA expression. Thus, the S protein is sufficient to cause inflammation that resembles what occurs

in patients with COVID-19. Our findings are consistent with a study that reported the N protein could also mimic inflammation that occurs in COVID-19.<sup>61</sup> Interestingly, after the addition of the N protein to A549 cells, a lung epithelial cell line, the authors observed overproduction of different cytokines relative to our study: IL-5, IL-15, IL-16, IP-10, macrophage inflammatory protein 1 $\alpha$  (MIP-1 $\alpha$ ), fibroblast growth factor (FGF) and eotaxin.<sup>61</sup> Xia et al showed that another coronavirus protein, envelope 2-E, administered into the tail vein of mice caused lung and spleen damage and a strong immune response associated with the cation channel.<sup>62</sup> Zhang et al reported similar results: both the S protein and only its ACE2 RBD increased the release of IL-6 and IL-8 from the human bronchial epithelium.<sup>21</sup> In another study, exposure of IB3-1 bronchial epithelial cells to the S protein increased the release of IL-6, IL-8, IL-9, FGF, G-CSF, GM-CSF, MCP-1 and MIP-1 $\beta$ ,<sup>22</sup> similarly to what we showed for HNEpCs. Surprisingly, the inflammatory effect of the S protein is similar to that exerted by lipopolysaccharide, which induced the expression of IL-8 and IL-6 in fibroblasts derived from nasal tissue.<sup>63</sup>

In addition to the epithelial cells of the respiratory system, the S protein also affects macrophages, which are the key cytokine-producing cells. Wang et al<sup>64</sup> showed that the S protein caused overproduction of IL-6 and TNF- $\alpha$  in macrophages.<sup>64</sup> In our study, the S protein led to increased production of M-CSF, which is involved in macrophage differentiation.<sup>65</sup> Moreover, the S protein increased IL-6 and its receptor in the lung epithelium, changes that resemble the acute phase of SARS-CoV-2 infection. IL-6 and IL-8 released in the body act as chemoattractants and promote the influx of immune cells, including monocytes and neutrophils.<sup>21,59</sup> It is believed that during infection and in hospitalised patients, there is increased production of IL-10, MCP-1, IP-10,<sup>59</sup> IL-1 $\beta$ , IL-6, IL-17, TNF- $\alpha$ , MCP-1, Toll-like receptor 3 and Toll-like receptor 7.<sup>66</sup> Secreted cytokines lead to tissue damage through pathological remodelling of the extracellular matrix (ECM). Metalloproteinases and their inhibitors (TIMPs) play a key role in lung diseases by altering the ECM. TIMP-1 circulating in the serum is associated with the severe course of COVID-19.<sup>67</sup> These reports have demonstrated that the use of the full-length S protein at a concentration of 2  $\mu$ g/mL can mimic the first stage of viral infection and justify our use of this model to investigate the protective function of fullerene and ectoine. The emergence of new SARS-CoV-2 variants is associated with the high mutability of the S protein. For this reason, vaccines have shown limited effectiveness over time. During the COVID-19 pandemic, distance, disinfection and masks have been utilised to limit the spread of the virus and interpersonal contacts. We used fullerene and ectoine together for the first time to develop a potential intranasal prophylactic medical device, namely an aqueous, moisturising and protective coating made of ectoine particles together with fullerene nanoparticles with high affinity for proteins.

Fullerene and its derivatives have previously shown antiviral activity against human immunodeficiency virus, respiratory syncytial virus (RSV), cytomegalovirus and others.<sup>68</sup> Given the high similarity of RSV to SARS-CoV-2 in terms of genetic material (an RNA virus), structure (an enveloped virus) and tissue tropism (respiratory system), we assumed that C<sub>60</sub> would also be effective for COVID-19 treatment. Consistently, in the fullerene treatment groups, there was a reduction in ACE2 expression on the surface of HNEpCs. This effect is probably related to the occupation of the active site by the fullerene core and reduced expression of the M pro-cysteine protease, as reported previously for fullerene with malonic acid. However, oxygen groups on the fullerene surface weaken the inhibition of enzymes involved in cleaving the S protein into the S1 and S2 subunits.<sup>69</sup> In our study, fullerene (58.65% oxygen and 39.79% carbon) decreased ACE2 expression on the surface of HNEpCs exposed to the S protein. It can be assumed that fullerene crystals (79.6 nm) with a size similar to the S protein (96.7 nm) and the same negative charge may occupy the ACE2 active sites to which the S protein binds. According to Page et al,<sup>70</sup> the RBD contains a cluster of positively charged amino acid residues that can interact electrostatically with the negatively charged fullerene.<sup>70</sup> Similar data were also obtained for graphene oxide, which showed affinity for unbound S protein and ACE2.<sup>71</sup> Moreover, Ershova et al<sup>26</sup> reported that fullerene did not accumulate inside cells during the first hours after addition, allowing time for it to interact with the cell membrane or other molecules.<sup>26</sup> We have provided evidence that ectoine itself increased the stability of the S protein to higher temperatures in culture, which resulted in even higher ACE2 expression than in the positive control (the S protein). After being broken down into intermediates, an unstable S protein may lose its ability to recognise ACE2 and to fuse with the membrane. An ectoine molecule, which is much smaller than fullerene C<sub>60</sub>, contains nitrogen incorporated into the carbon ring and probably protects the second- and third-order structure of the S protein, limiting its aggregation and surrounding it with a water shell.<sup>72</sup> Ectoine could be important for the treatment of inflammatory

conditions of the nasal cavity with reduced ACE2 expression, including chronic rhinosinusitis with nasal polyps.<sup>73</sup> Using dynamic light scattering, we confirmed that ectoine limited the agglomeration of the S protein as well as fullerene particles in the fullerene–ectoine composite. Given that increased ACE2 expression in the olfactory neuroepithelium is associated with anosmia as well as SARS-CoV-2 entry and replication,<sup>74</sup> we hypothesise that a fullerene–ectoine composite captures and traps the S protein and prevents it from binding to ACE2, thus protecting the nasal epithelium against uncontrolled production of inflammatory cytokines. Our results support this hypothesis: HNEpCs pretreated with MIX low followed by the S protein showed similar secretion of IL-6, MCP-1, MCP-2, TIMP-2, M-CSF, IL-8 and eotaxin as the negative control, and lower secretion compared with the positive control. Further, there was lower MCP-1, TIMP-2, ICAM and IL-8 gene expression in these cells compared with the negative control. Of note, researchers showed that fullerene inhibits inflammation and degeneration in the vertebral bone marrow and explained this by its antioxidant and anti-inflammatory properties.<sup>75</sup>

IL-6 damages the lungs. High levels occur in patients with COVID-19 requiring mechanical ventilation and oxygen.<sup>76</sup> For this reason, IL-6 is the target of many drugs that alleviate COVID-19 symptoms, such as tocilizumab, sirukumab, sarilumab and siltuximab.<sup>77</sup> This cytokine is associated with allergic rhinitis, olfactory dysfunction due to coronaviruses and Sjögren's syndrome, and cancer. It participates in the janus kinases/signal transducer and activator of transcription 3 (JAK/STAT3) and nuclear factor  $\kappa$ B (NF- $\kappa$ B) signalling pathways in which cells ignore apoptotic signals and proliferate rapidly by binding to the membrane-bound receptor IL-6R $\alpha$  and gp130 (the cis pathway).<sup>78,79</sup> We showed that IL-6 secretion by HNEpCs was reduced after the addition of the fullerene–ectoine composite compared with the positive control, but IL-6 gene expression was increased. One possible reason is that cells sensing low levels of IL-6 in the ECM increase IL-6 gene expression via a feedback loop. In another study, stimulation of HNEpCs with IL-6 accelerated wound closure and cilia beating. IL-6 is also involved in the extracellular signal-regulated kinase 1/2 pathway, through which it regulates the production of metalloproteinases.<sup>80</sup> We found that reduced extracellular IL-6 was accompanied by decreased extracellular TIMP-2 expression. This inhibitor is responsible for the inactivation of zinc-dependent endopeptidases capable of degrading ECM components. Reduced TIMP-2 levels activate matrix metalloproteinase 2 (MMP2), but we did not examine this protein. According to the literature, high levels of angiotensin II increase MMP-2.<sup>81</sup> We demonstrated that the fullerene–ectoine composite reduced the expression of ACE2, a phenomenon that is associated with low levels of angiotensin II and MMP2 and correlates with reduced swelling and lack of secretion on the nasal mucosa.<sup>81,82</sup> Moreover, there were increased circulating MMP9/TIMP-1 and MMP2/TIMP-2 ratios in patients with COVID-19 2 weeks after recovery from the acute phase, with high MMP9 levels dominating in critical COVID-19.<sup>83</sup> The TIMP levels also depend on the characteristics of the tissue from which the cells were collected. For example, low TIMP-2 levels have been observed in nasal polyps, and high TIMP-2 levels have been observed in patients with allergic rhinitis after allergen challenge.<sup>81</sup>

IL-6 also participates in trans signalling by binding to the soluble form of its receptor (sIL-6R) to regulate the IL network. It increases the secretion of IL-8, vascular endothelial growth factor and MCP-1, and reduces E-cadherin levels.<sup>84</sup> IL-8 binds to G protein-coupled CXC chemokine receptors (CXCR1 and CXCR2), which activate chemotaxis and accumulation of neutrophils in tissues. High IL-8 levels in lung tissue correlate negatively with lung function. Potential antibacterial and antiviral drugs targeting the IL-8/CXCR1/CXCR2 pathway have been sought.<sup>85</sup> Fullerene C<sub>60</sub>, with antioxidant activity comparable to  $\alpha$ -tocopherol, plays a cytoprotective role in biological systems.<sup>86</sup> A composite containing 10 mg/L fullerene reduced IL-8. Human epidermal keratinocytes exposed to 42.5  $\mu$ g/mL C<sub>60</sub>(OH)<sub>24</sub> and C<sub>60</sub>(OH)<sub>32</sub> for 24 or 48 h showed a decrease in IL-8; there were no changes in the C<sub>60</sub>(OH)<sub>20</sub> group. The authors explained these results based on the adsorption of IL-8 on the fullerene surface. Moreover, IL-8 suppression increased as hydroxylation of fullerene and its concentration increased.<sup>86</sup> Ectoine also has a proven anti-inflammatory effect. The commercially available inhalation solution under the trade name Ectoin<sup>®</sup> reduced IL-8, nitric oxide and the number of neutrophils in sputum collected from people with mild symptoms of respiratory diseases during the first period of treatment.<sup>87</sup>

We found that the MCP-1 and MCP-2 levels were normalised to those of the negative control by preincubating HNEpCs with the fullerene–ectoine composite followed by exposure to the S protein. According to Kovarik et al,<sup>88</sup> these chemokines are produced by fibroblasts, monocytes and macrophages and use many cell receptors to attract and mature monocytes. Due to the fact that the nasal mucosa is highly vascularised,<sup>89</sup> MCP expression seems to be quite

important. Previously, analysis of serum from 55 patients with SARS-CoV-2 infection showed high levels of MCP-2.<sup>88</sup> According to the literature, pristine fullerene C<sub>60</sub> increased MCP-1 mRNA expression in mouse lung tissue after intratracheal instillation, although the increase was significantly lower compared with single-wall carbon nanotubes and quantum dots.<sup>90</sup> However, in the same study, fullerene inhalation did not change MCP-1 levels, similar to our findings regarding MCP-1 and MCP-2 levels in the culture medium.

M-CSF is also important for the recruitment of immune system cells. Next to IL-6, M-CSF is the main factor involved in the severe course of COVID-19, pneumonia and organ damage.<sup>77</sup> The serum of patients collected 1 month after SARS-CoV-2 infection contained more M-CSF compared with the reference level.<sup>91</sup> Preincubation of HNEpCs with the fullereneol–ectoine composite followed by exposure to the S protein did not change the M-CSF levels in the HNEpC culture medium compared with the negative control. These results are consistent with our previous work, where the same fullereneol did not affect M-CSF in healthy and cancer cells of the liver.<sup>25</sup> In contrast, there are limited data regarding the effect of ectoine on M-CSF.

ICAM-1, also known as CD54, is an immunoglobulin, a transmembrane protein responsible for intercellular adhesion. Takeuchi et al<sup>92</sup> reported that ICAM-1 may contribute to the binding of the S1 subunit to the olfactory epithelium of the nasal cavity of mice. Bałaban et al<sup>3</sup> reported an increase in ICAM-1 after adding 5 µg/mL of the S protein. Therefore, the reduced ICAM-1 mRNA expression in response to pretreatment with the fullereneol–ectoine composite may be associated with a weaker interaction between the S protein and the cell membrane. A reduction in ICAM-1 was demonstrated after adding diamond<sup>93</sup> and graphene oxide<sup>3,93</sup> to pancreatic cells and muscle fibres. For fullereneols, the situation is not so simple: the amount of oxygen on the surface of the particles is particularly important, which translates into the activation<sup>94</sup> or inhibition of ICAM-1.<sup>95</sup> According to Gelderman et al,<sup>94</sup> the use of fullereneol C<sub>60</sub>(OH)<sub>24</sub> induced the pro-inflammatory activity of vascular endothelial cells, which resulted in an increase in ICAM-1 expression.<sup>94</sup> In another study, C<sub>60</sub>(OH)<sub>36</sub> fullereneol, which has a similar number of hydroxyl groups as the fullereneol we used, reduced the level of ICAM-1 and counteracted the cytotoxicity of HaCaT cells (a keratinocyte cell line) induced by the addition of urban particulate matter.<sup>95</sup> We found that the effect of fullereneol was enhanced by the addition of ectoine. According to a previous study, ectoine reduced ICAM-1 in a colitis model.<sup>96</sup>

In summary, FTIR and EDS analysis confirmed the presence of carbon and oxygen in fullereneol and carbon, oxygen, and nitrogen in ectoine, which indicated the purity of the materials used. After 24 h, only 2% ectoine caused a decrease in the conversion of XTT to formazan in HNEpC cells and a tendency to form large clusters. We found that 10 mg/L fullereneol, 0.2% ectoine and their composite are fully biocompatible and do not affect the level of mucins. However, the viability of HNEpC cells depended on the dose of ectoine and fullereneol and the incubation time. The results of XTT and DCF-DA suggest that the spike ranging in size from 75 to 120 nm at a concentration of 2 µg/mL decreases metabolic activity and induces oxidative stress of epithelial nasal cells. Confocal microscopy shows that fullereneol reduced and ectoine increased ACE2 surface area on HNEpCs. In the present study, cytokine analysis using RT-PCR and chemiluminescent protein membranes showed that the cytokine profile level was similar in the negative control group and group spike-treated after precoated cells by fullereneol and ectoine. All these data indicated that fullereneol and ectoine might be attractive mechanical shell for nasal mucosa until it is fully regenerated.

## Conclusion

We hypothesised that a fullereneol–ectoine composite is a safe intranasal medical device that protects HNEpCs against the first phase of SARS-CoV-2 infection. We demonstrated that 10, 50 and 100 mg/L fullereneol and 0.2% and 1% ectoine and their composites are biocompatible after 24 h incubation with HNEpCs. The fullereneol–ectoine composite was dominated by carbon and nitrogen, followed by oxygen, and fullereneol showed a lower tendency to agglomerate when combined with ectoine. Next, we mimicked SARS-CoV-2 infection by treating HNEpCs with the full-length S protein. At a concentration of 2 µg/mL, the S protein reduced the mitochondrial activity of HNEpCs and increased intracellular ROS after 24 h. Moreover, the S increased ACE2 expression on the surface of HNEpCs; the secretion of cytokines IL-6, MCP-1, TIMP-2, M-CSF, IL-8; and IL-6 and TIMP-2 gene expression. Finally, we demonstrated that preincubation of HNEpCs with the 10 mg/L fullereneol–0.2% ectoine composite for 1 h protected them against the S protein – perhaps by preventing the S protein–ACE2 interaction – and maintained cytokine levels similar to those of the negative control. In

the future, we will evaluate the effect of the fullerene–ectoine composite on the other coronavirus proteins (E, M or N) and OC43 human coronavirus and in animals. Confirmation of the results we have reported here could lead to the availability of the first medical device with a function similar to protective masks, supporting damaged, thin nasal epithelium after previous viral and bacterial infections.

## Acknowledgments

This research was funded by the National Science Centre Poland, grant number 2019/33/N/NZ7/01392. This report is a part of Malwina Sosnowska's habilitation thesis.

## Author Contributions

All authors made a significant contribution to the work reported, whether that is in the conception, study design, execution, acquisition of data, analysis and interpretation, or in all these areas; took part in drafting, revising or critically reviewing the article; gave final approval of the version to be published; have agreed on the journal to which the article has been submitted; and agree to be accountable for all aspects of the work.

## Disclosure

Dr Malwina Sosnowska, Prof Mateusz Wierzbicki, Dr Barbara Strojny-Cieślak, Prof Ewa Sawosz and Dr Marta Kutwin report a pending patent “Composition with barrier and virucidal properties against coronaviruses, especially SARS-CoV-2, method of obtaining it and use” (Poland patent pending, number P.448505). The authors declare no conflict of interest in this work.

## References

1. Beyerstedt S, Casaro EB, Rangel ÉB. COVID-19: angiotensin-converting enzyme 2 (ACE2) expression and tissue susceptibility to SARS-CoV-2 infection. *Eur J Clin Microbiol Infect Dis*. 2021;40(5):905–919. doi:10.1007/s10096-020-04138-6
2. Heidary M, Kaviar VH, Shirani M, et al. A comprehensive review of the protein subunit vaccines against COVID-19. *Front Microbiol*. 2022;13:927306. doi:10.3389/fmicb.2022.927306
3. Bałaban J, Wierzbicki M, Zielińska-Górska M, et al. Graphene oxide decreases pro-inflammatory proteins production in skeletal muscle cells exposed to SARS-CoV-2 spike protein. *Nanotechnol Sci Appl*. 2023;16:1–18. doi:10.2147/NSA.S391761
4. Touisserkani SK, Ayatollahi A. Oral corticosteroid relieves post-COVID-19 anosmia in a 35-year-old patient. *Case Rep Otolaryngol*. 2020;2020:5892047. doi:10.1155/2020/5892047
5. Parisi GF, Brindisi G, Indolfi C, et al. COVID-19, anosmia, and ageusia in atopic children. *Pediatr Allerg Immunol*. 2022;33:99–101. doi:10.1111/pai.13644
6. Zhu F, Teng Z, Zhou X, et al. H1N1 influenza virus-infected nasal mucosal epithelial progenitor cells promote dendritic cell recruitment and maturation. *Front Immunol*. 2022;13:879575. doi:10.3389/fimmu.2022.879575
7. Sanli DET, Altundag A, Kandemirli SG, et al. Relationship between disease severity and serum IL-6 levels in COVID-19 anosmia. *Am J Otolaryng*. 2021;42(1):102796. doi:10.1016/j.amjoto.2020.102796
8. Doty RL. The mechanisms of smell loss after SARS-CoV-2 infection. *Lancet Neurol*. 2021;20(9):693–695. doi:10.1016/S1474-4422(21)00202-7
9. Khatiwada S, Subedi A. A mechanistic link between selenium and coronavirus disease 2019 (COVID-19). *Curr Nutr Rep*. 2021;10:125–136. doi:10.1007/s13668-021-00354-4
10. Abdelsalam YI, Aliev FA, Khamidullin RF, Dengaev AV, Katnov VE, Vakhin AV. Catalytic low-temperature thermolysis of heavy oil in the presence of fullerene c60 nanoparticles in aquatic and N2 medium. *Catalysts*. 2023;13(2):347. doi:10.3390/catal13020347
11. Sayers BC, Germolec DR, Walker NJ, et al. Respiratory toxicity and immunotoxicity evaluations of microparticle and nanoparticle C60 fullerene aggregates in mice and rats following nose-only inhalation for 13 weeks. *Nanotoxicology*. 2016;10(10):1458–1468. doi:10.1080/17435390.2016.1235737
12. Taylor R. Addition reactions of fullerenes. *CR Chim*. 2006;9(7–8):982–1000. doi:10.1016/j.crci.2006.01.004
13. Chen X, Yang J, Li M, et al. Fullerene protects cornea from ultraviolet B exposure. *Redox Biol*. 2022;54:102360. doi:10.1016/j.redox.2022.102360
14. Injac R, Prijatelj M, Strukelj B. Fullerene nanoparticles: toxicity and antioxidant activity. *Methods Mol Biol*. 2013;1028:75–100. doi:10.1007/978-1-62703-475-3\_5
15. Xu JY, Han K, Li SX, et al. Pulmonary responses to polyhydroxylated fullerenols, C60(OH)<sub>x</sub>. *J Appl Toxicol*. 2009;29(7):578–584. doi:10.1002/jat.1442
16. Jiao X, Wang Z, Li Y, et al. Fullerene inhibits tendinopathy by alleviating inflammation. *Front Bioeng Biotechnol*. 2023;11:1171360. doi:10.3389/fbioe.2023.1171360
17. Dao VA, Overhagen S, Bilstein A, Kolot C, Sonnemann U, Mösges R. Ectoine lozenges in the treatment of acute viral pharyngitis: a prospective, active-controlled clinical study. *Eur Arch Otorhinolaryngol*. 2019;276:775–783. doi:10.1007/s00405-019-05324-9
18. Kocherovets VI. Ectoine — a microbial metabolite with unique biotherapeutic properties. *Pediatric Consilium Medicum*. 2019;1:108–115.
19. Hui H, Ma W, Cui J, et al. Periodic acid-Schiff staining method for function detection of liver cells is affected by 2% horse serum in induction medium. *Mol Med Rep*. 2017;16(6):8062–8068. doi:10.3892/mmr.2017.7587



20. Tanne C, Golovina EA, Hoekstra FA, Meffert A, Galinski EA. Glass-forming property of hydroxyectoine is the cause of its superior function as a desiccation protectant. *Front Microbiol.* 2014;5:150. doi:10.3389/fmicb.2014.00150
21. Zhang RG, Liu XJ, Guo YL, Chen CL. SARS-CoV-2 spike protein receptor binding domain promotes IL-6 and IL-8 release via ATP/P2Y2 and ERK1/2 signaling pathways in human bronchial epithelia. *Mol Immunol.* 2024;167:53–61. doi:10.1016/j.molimm.2024.02.005
22. Gasparello J, d'Aversa E, Breveglieri G, Borgatti M, Finotti A, Gambari R. In vitro induction of interleukin-8 by SARS-CoV-2 Spike protein is inhibited in bronchial epithelial IB3-1 cells by a miR-93-5p agomiR. *Int Immunopharmacol.* 2021;101:108201. doi:10.1016/j.intimp.2021.108201
23. Sosnowska-Iawnicka M, Kutwin M, Sawosz-Chwalibóg E, et al. Composition with barrier and virucidal properties against coronaviruses, especially SARS-CoV-2, method of its preparation and use. Poland patent P.448505; 2024.
24. Schramm F, Lange M, Hoppmann P, Heutelbeck A. Cytotoxicity of carbon nanohorns in different human cells of the respiratory system. *J Toxicol Environ Heal A.* 2016;79(22–23):1085–1093. doi:10.1080/15287394.2016.1219594
25. Sosnowska M, Kutwin M, Koczoń P, Chwalibog A, Sawosz E. Polyhydroxylated fullerene C<sub>60</sub>(OH)<sub>40</sub> nanofilms promote the mesenchymal–epithelial transition of human liver cancer cells via the TGF-β1/Smad pathway. *J Inflamm Res.* 2023;16:3739–3761. doi:10.2147/JIR.S415378
26. Ershova ES, Sergeeva VA, Chausheva AI, et al. Toxic and DNA damaging effects of a functionalized fullerene in human embryonic lung fibroblasts. *Mutat Res Genet Toxicol Environ Mutagen.* 2016;805:46–57. doi:10.1016/j.mrgentox.2016.05.004
27. Wang F, Jin C, Liang H, Tang Y, Zhang H, Yang Y. Effects of fullerene C60 nanoparticles on A549 cells. *Environ Toxicol Phar.* 2014;37(2):656–661. doi:10.1016/j.etap.2014.01.015
28. Chen YW, Hwang KC, Yen CC, Lai YL. Fullerene derivatives protect against oxidative stress in RAW 264.7 cells and ischemia-reperfused lungs. *Am J Physiol Regul Integr Comp Physiol.* 2004;287(1):R21–R26. doi:10.1152/ajpregu.00310.2003
29. Su Y, Xu JY, Shen P, et al. Cellular uptake and cytotoxic evaluation of fullereneol in different cell lines. *Toxicology.* 2010;269(2–3):155–159. doi:10.1016/j.tox.2009.11.015
30. Çavaş T, Çinkılıç N, Vatan Ö, Yılmaz D. Effects of fullereneol nanoparticles on acetamiprid induced cytotoxicity and genotoxicity in cultured human lung fibroblasts. *Pestic Biochem Phys.* 2014;114:1–7. doi:10.1016/j.pestbp.2014.07.008
31. Rieckmann T, Gatzemeier F, Christiansen S, Rothkamm K, Münscher A. The inflammation-reducing compatible solute ectoine does not impair the cytotoxic effect of ionizing radiation on head and neck cancer cells. *Sci Rep.* 2019;9(1):6594. doi:10.1038/s41598-019-43040-w
32. Yao CL, Lin YM, Mohamed MS, Chen JH. Inhibitory effect of ectoine on melanogenesis in B16-F0 and A2058 melanoma cell lines. *Biochem Eng J.* 2013;78:163–169. doi:10.1016/j.bej.2013.01.005
33. Fatollahi P, Ghasemi M, Yazdian F, Sadeghi A. Ectoine production in bioreactor by *Halomonas elongata* DSM2581: using MWCNT and Fe-nanoparticle. *Biotechnol Progr.* 2021;37(1):e3073. doi:10.1002/btpr.3073
34. Autengruber A, Sydlik U, Kroker M, et al. Signalling-dependent adverse health effects of carbon nanoparticles are prevented by the compatible solute mannosylglycerate (firoin) in vitro and in vivo. *PLoS One.* 2014;9(11):e111485. doi:10.1371/journal.pone.0111485
35. Barzegar A, Mousavi SJ, Hamidi H, Sadeghi M. 2D-QSAR study of fullerene nanostructure derivatives as potent HIV-1 protease inhibitors. *Physica E.* 2017;93:324–331. doi:10.1016/j.physe.2017.06.016
36. Innocenzi P, Stagi L. Carbon-based antiviral nanomaterials: graphene, C-dots, and fullerenes. A perspective. *Chem Sci.* 2020;11(26):6606–6622. doi:10.1039/D0SC02658A
37. Prylutskyi YI, Cherepanov VV, Evstigneev MP, et al. Structural self-organization of C60 and cisplatin in physiological solution. *Phys Chem Chem Phys.* 2015;17(39):26084–26092. doi:10.1039/C5CP02688A
38. Meyer S, Schröter MA, Hahn MB, Solomun T, Sturm H, Kunte HJ. Ectoine can enhance structural changes in DNA in vitro. *Sci Rep.* 2017;7(1):7170. doi:10.1038/s41598-017-07441-z
39. Butowska K, Kozak W, Zdrochowicz M, et al. Cytotoxicity of doxorubicin conjugated with C60 fullerene. Structural and in vitro studies. *Struct Chem.* 2019;30(6):2327–2338. doi:10.1007/s11224-019-01428-4
40. Yang N, Cheng H, Mo Q, Zhou X, Xie M. miR-155-5p downregulation inhibits epithelial-to-mesenchymal transition by targeting SIRT1 in human nasal epithelial cells. *Mol Med Rep.* 2020;22(5):3695–3704. doi:10.3892/mmr.2020.11468
41. Castro-Ochoa KF, Vargas-Robles H, Cháñez-Paredes S, et al. Homoectoine protects against colitis by preventing a claudin switch in epithelial tight junctions. *Digest Dis Sci.* 2019;64:409–420. doi:10.1007/s10620-018-5309-8
42. Carlson TL, Lock JY, Carrier RL. Engineering the mucus barrier. *Annu Rev Biomed Eng.* 2018;20:197–220. doi:10.1146/annurev-bioeng-062117-121156
43. Sun B, Wang B, Xu M. Esculetin inhibits histamine-induced expression of inflammatory cytokines and mucin in nasal epithelial cells. *Clin Exp Pharmacol Physiol.* 2019;46(9):821–827. doi:10.1111/1440-1681.13128
44. Ishinaga H, Kitano M, Toda M, et al. Interleukin-33 induces mucin gene expression and goblet cell hyperplasia in human nasal epithelial cells. *Cytokine.* 2017;90:60–65. doi:10.1016/j.cyto.2016.10.010
45. Suzuki YJ, Nikolaienko SI, Dibrova VA, et al. SARS-CoV-2 spike protein-mediated cell signaling in lung vascular cells. *Vasc Pharmacol.* 2021;137:106823. doi:10.1016/j.vph.2020.106823
46. Buzhdygan TP, DeOre BJ, Baldwin-Leclair A, et al. The SARS-CoV-2 spike protein alters barrier function in 2D static and 3D microfluidic in-vitro models of the human blood–brain barrier. *Neurobiol Dis.* 2020;146:105131. doi:10.1016/j.nbd.2020.105131
47. Clough E, Inigo J, Chandra D, et al. Mitochondrial dynamics in SARS-COV2 spike protein treated human microglia: implications for neuro-COVID. *J Neuroimmune Pharm.* 2021;16:770–784. doi:10.1007/s11481-021-10015-6
48. Manfredelli D, Pariano M, Costantini C, et al. Severe acute respiratory syndrome coronavirus 2 (SARS-CoV-2) spike protein S1 induces methylglyoxal-derived hydroimidazolone/receptor for advanced glycation end products (MG-H1/RAGE) activation to promote inflammation in human bronchial BEAS-2B cells. *Int J Mol Sci.* 2023;24(19):14868. doi:10.3390/ijms241914868
49. Keturakis V, Naruskaitė D, Balion Z, et al. The effect of SARS-CoV-2 spike protein RBD-epitope on immunometabolic state and functional performance of cultured primary cardiomyocytes subjected to hypoxia and reoxygenation. *Int J Mol Sci.* 2023;24(23):16554. doi:10.3390/ijms242316554
50. Perico L, Morigi M, Pezzotta A, et al. SARS-CoV-2 spike protein induces lung endothelial cell dysfunction and thrombo-inflammation depending on the C3a/C3a receptor signalling. *Sci Rep.* 2023;13(1):11392. doi:10.1038/s41598-023-38382-5

51. Youn JY, Zhang Y, Wu Y, Cannesson M, Cai H. Therapeutic application of estrogen for COVID-19: attenuation of SARS-CoV-2 spike protein and IL-6 stimulated, ACE2-dependent NOX2 activation, ROS production and MCP-1 upregulation in endothelial cells. *Redox Biol.* 2021;46:102099. doi:10.1016/j.redox.2021.102099
52. Zhang Y, Peng X, Xue M, et al. SARS-COV-2 spike protein promotes RPE cell senescence via the ROS/P53/P21 pathway. *Biogerontology.* 2023;24(5):813–827. doi:10.1007/s10522-023-10019-0
53. Li F, Li J, Wang PH, et al. SARS-CoV-2 spike promotes inflammation and apoptosis through autophagy by ROS-suppressed PI3K/AKT/mTOR signaling. *Biochim Biophys Acta Mol Basis Dis.* 2021;1867(12):166260. doi:10.1016/j.bbdis.2021.166260
54. Poeta M, Cioffi V, Tarallo A, et al. Postbiotic preparation of Lacticaseibacillus rhamnosus GG against diarrhea and oxidative stress induced by spike protein of SARS-CoV-2 in human enterocytes. *Antioxidants.* 2023;12(10):1878. doi:10.3390/antiox12101878
55. Jiang J, Gu X, Song R, et al. Time-dependent oxidative stress and histopathological changes in *Cyprinus carpio* L. exposed to microcystin-LR. *Ecotoxicology.* 2011;20:1000–1009. doi:10.1007/s10646-011-0646-9
56. Murphy MP, Bayir H, Belousov V, et al. Guidelines for measuring reactive oxygen species and oxidative damage in cells and in vivo. *Nat Metab.* 2022;4(6):651–662. doi:10.1038/s42255-022-00591-z
57. Poeta M, Cioffi V, Buccigrossi V, et al. SARS-CoV-2 causes secretory diarrhea with an enterotoxin-like mechanism, which is reduced by diosmectite. *Heliyon.* 2022;8(8):e10246. doi:10.1016/j.heliyon.2022.e10246
58. Zhou Y, Wang M, Li Y, et al. SARS-CoV-2 Spike protein enhances ACE2 expression via facilitating Interferon effects in bronchial epithelium. *Immunol Lett.* 2021;237:33–41. doi:10.1016/j.imlet.2021.06.008
59. Patra T, Meyer K, Geerling L, et al. SARS-CoV-2 spike protein promotes IL-6 trans-signaling by activation of angiotensin II receptor signaling in epithelial cells. *PLoS Pathog.* 2020;16(12):e1009128. doi:10.1371/journal.ppat.1009128
60. Eichhorn T, Huber S, Weiss R, et al. Infection with SARS-CoV-2 is associated with elevated levels of IP-10, MCP-1, and IL-13 in sepsis patients. *Diagnostics.* 2023;13(6):1069. doi:10.3390/diagnostics13061069
61. Wang YC, Tsai CH, Wang YC, et al. SARS-CoV-2 nucleocapsid protein, rather than spike protein, triggers a cytokine storm originating from lung epithelial cells in patients with COVID-19. *Infection.* 2023;52(3):955–983. doi:10.1007/s15010-023-02142-4
62. Xia B, Shen X, He Y, et al. SARS-CoV-2 envelope protein causes acute respiratory distress syndrome (ARDS)-like pathological damages and constitutes an antiviral target. *Cell Res.* 2021;31(8):847–860. doi:10.1038/s41422-021-00519-4
63. Xing Z, Jordana M, Braciak T, Ohtoshi T, Gaudie J. Lipopolysaccharide induces expression of granulocyte/macrophage colony-stimulating factor, interleukin-8, and interleukin-6 in human nasal, but not lung, fibroblasts: evidence for heterogeneity within the respiratory tract. *Am J Resp Cell Mol.* 1993;9:255–263. doi:10.1165/ajrcmb/9.3.255
64. Wang W, Ye L, Ye L, et al. Up-regulation of IL-6 and TNF- $\alpha$  induced by SARS-coronavirus spike protein in murine macrophages via NF- $\kappa$ B pathway. *Virus Res.* 2007;128(1–2):1–8. doi:10.1016/j.virusres.2007.02.007
65. Duarte C, Akkaoui J, Ho A, Garcia C, Yamada C, Movila A. Age-dependent effects of the recombinant spike protein/SARS-CoV-2 on the M-CSF- and IL-34-differentiated macrophages in vitro. *Biochem Bioph Res Commun.* 2021;546:97–102. doi:10.1016/j.bbrc.2021.01.104
66. Petrone V, Fanelli M, Giudice M, et al. Expression profile of HERVs and inflammatory mediators detected in nasal mucosa as a predictive biomarker of COVID-19 severity. *Front Microbiol.* 2023;14:1155624. doi:10.3389/fmicb.2023.1155624
67. Brusa S, Terracciano D, Bruzzese D, et al. Circulating tissue inhibitor of metalloproteinases 1 (TIMP-1) at COVID-19 onset predicts severity status. *Front Med.* 2022;9:1034288. doi:10.3389/fmed.2022.1034288
68. Falynskova IN, Ionova KS, Dedova AV, Leneva IA, Makhmudova NR, Rasnetsov LD. Antiviral activity of fullerene-(tris-aminocaproic acid) hydrate against respiratory syncytial virus in HEp-2 cell culture. *Pharm Chem J.* 2014;48:85–88. doi:10.1007/s11094-014-1053-3
69. Katagishi D, Yasuda D, Takahashi K, Nakamura S, Mashino T, Ohe T. Fullerene derivatives as inhibitors of the SARS-CoV-2 main protease. *Bioorg Med Chem Lett.* 2023;80:129121. doi:10.1016/j.bmcl.2022.129121
70. Page TM, Nie C, Neander L, et al. Functionalized fullerene for inhibition of SARS-CoV-2 variants. *Small.* 2023;19(15):2206154. doi:10.1002/sml.202206154
71. Unal MA, Bayrakdar F, Nazir H, et al. Graphene oxide nanosheets interact and interfere with SARS-CoV-2 surface proteins and cell receptors to inhibit infectivity. *Small.* 2021;17(25):2101483. doi:10.1002/sml.202101483
72. Salmannejad F, Nafissi-Varcheh N. Ectoine and hydroxyectoine inhibit thermal-induced aggregation and increase thermostability of recombinant human interferon Alfa2b. *Eur J Pharm Sci.* 2017;97:200–207. doi:10.1016/j.ejps.2016.11.014
73. Takabayashi T, Yoshida K, Imoto Y, Schleimer RP, Fujieda S. Regulation of the expression of SARS-CoV-2 receptor angiotensin-converting enzyme 2 in nasal mucosa. *Am J Rhinol Allergy.* 2022;36(1):115–122. doi:10.1177/19458924211027798
74. Chen M, Shen W, Rowan NR, et al. Elevated ACE-2 expression in the olfactory neuroepithelium: implications for anosmia and upper respiratory SARS-CoV-2 entry and replication. *Eur Respir J.* 2020;56(3):2001948. doi:10.1183/13993003.01948-2020
75. Liu Q, Jin L, Shen FH, Balian G, Li XJ. Fullerol nanoparticles suppress inflammatory response and adipogenesis of vertebral bone marrow stromal cells—a potential novel treatment for intervertebral disc degeneration. *Spine J.* 2013;13(11):1571–1580. doi:10.1016/j.spinee.2013.04.004
76. Santa Cruz A, Mendes-Frias A, Oliveira AI, et al. Interleukin-6 is a biomarker for the development of fatal severe acute respiratory syndrome coronavirus 2 pneumonia. *Front Immunol.* 2021;12:613422. doi:10.3389/fimmu.2021.613422
77. Quartuccio L, Fabris M, Sonaglia A, et al. Interleukin 6, soluble interleukin 2 receptor alpha (CD25), monocyte colony-stimulating factor, and hepatocyte growth factor linked with systemic hyperinflammation, innate immunity hyperactivation, and organ damage in COVID-19 pneumonia. *Cytokine.* 2021;140:155438. doi:10.1016/j.cyto.2021.155438
78. Xiao Y, Qian J, Deng X, et al. Macrophages regulate healing-associated fibroblasts in diabetic wound. *Mol Biol Rep.* 2024;51(1):203. doi:10.1007/s11033-023-09100-1
79. Mukherjee A, Khuda-Bukhsh AR. Quercetin down-regulates IL-6/STAT-3 signals to induce mitochondrial-mediated apoptosis in a non-small-cell lung-cancer cell line, A549. *J Pharmacopuncture.* 2015;18(1):19. doi:10.3831/KPI.2015.18.002
80. Bequignon E, Mangin D, Bécud J, et al. Pathogenesis of chronic rhinosinusitis with nasal polyps: role of IL-6 in airway epithelial cell dysfunction. *J Transl Med.* 2020;18:1–12. doi:10.1186/s12967-020-02309-9
81. Mori S, Pawankar R, Ozu C, Nonaka M, Yagi T, Okubo K. Expression and roles of MMP-2, MMP-9, MMP-13, TIMP-1, and TIMP-2 in allergic nasal mucosa. *Allergy Asthma Immunol Res.* 2012;4(4):231. doi:10.4168/air.2012.4.4.231

82. Tikellis C, Thomas MC. Angiotensin-converting enzyme 2 (ACE2) is a key modulator of the renin angiotensin system in health and disease. *Int J Pept.* 2012;2012:256294. doi:10.1155/2012/256294
83. Cavalcante GL, Bonifacio LP, Sanches-lobes JM, et al. Matrix metalloproteinases are associated with severity of disease among COVID-19 patients: a possible pharmacological target. *Basic Clin Pharmacol.* 2024;134(5):727–736. doi:10.1111/bcpt.14001
84. Fatima SH, Viqar U, Ahmed T, Kazmi MH. The possible immunopathogenesis of SARS-Cov-2 infection-A review of immune changes in patients with COVID-19. *Indian J Pathol Oncol.* 2020;7(4):519–526. doi:10.18231/j.ijpo.2020.105
85. Cesta MC, Zippoli M, Marsiglia C, et al. The role of interleukin-8 in lung inflammation and injury: implications for the management of COVID-19 and hyperinflammatory acute respiratory distress syndrome. *Front Pharmacol.* 2022;12:808797. doi:10.3389/fphar.2021.808797
86. Saathoff JG, Inman AO, Xia XR, Riviere JE, Monteiro-Riviere NA. In vitro toxicity assessment of three hydroxylated fullerenes in human skin cells. *Toxicol In Vitro.* 2011;25(8):2105–2112. doi:10.1016/j.tiv.2011.09.013
87. Unfried K, Krämer U, Sydlik U, et al. Reduction of neutrophilic lung inflammation by inhalation of the compatible solute ectoine: a randomized trial with elderly individuals. *Int J Chronic Obstruct Pulmon Dis.* 2016;11:2573–2583. doi:10.2147/COPD.S115061
88. Kovarik JJ, Kämpf AK, Gasser F, et al. Identification of immune activation markers in the early onset of COVID-19 infection. *Front Cell Infect Microbiol.* 2021;11:651484. doi:10.3389/fcimb.2021.651484
89. Gallo O, Locatello LG, Mazzoni A, Novelli L, Annunziato F. The central role of the nasal microenvironment in the transmission, modulation, and clinical progression of SARS-CoV-2 infection. *Mucosal Immunol.* 2021;14(2):305–316. doi:10.1038/s41385-020-00359-2
90. Jacobsen NR, Møller P, Jensen KA, et al. Lung inflammation and genotoxicity following pulmonary exposure to nanoparticles in ApoE<sup>-/-</sup> mice. *Part Fibre Toxicol.* 2009;6:1–17. doi:10.1186/1743-8977-6-2
91. Radaeva OA, Simbirtsev AS, Selezneva NM, Iskandryarova MS. Serum macrophage colony-stimulating factor levels in patients with essential hypertension after SARS-CoV-2 infection. *Russ J Immunol.* 2020;23(4):429–436. doi:10.46235/1028-7221-430-SMC
92. Takeuchi F, Sugano A, Yoneshige A, et al. Potential contribution of cell adhesion molecule 1 to the binding of SARS-CoV-2 spike protein to mouse nasal mucosa. *Cells Tissues Organs.* 2023;213(4):326–337. doi:10.1159/000534892
93. Wójcik B, Sawosz E, Szczepaniak J, et al. Effects of metallic and carbon-based nanomaterials on human pancreatic cancer cell lines AsPC-1 and BxPC-3. *Int J Mol Sci.* 2021;22(22):12100. doi:10.3390/ijms222212100
94. Gelderman MP, Simakova O, Clogston JD, et al. Adverse effects of fullerenes on endothelial cells: fullereneol C60(OH)24 induced tissue factor and ICAM-1 membrane expression and apoptosis in vitro. *Int J Nanomed.* 2008;3(1):59–68. doi:10.1182/blood.V108.11.1801.1801
95. Lee CW, Chi MC, Peng KT, et al. Water-soluble fullereneol C60(OH)36 toward effective anti-air pollution induced by urban particulate matter in HaCaT cell. *Int J Mol Sci.* 2019;20(17):4259. doi:10.3390/ijms20174259
96. Abdel-Aziz H, Wadie W, Abdallah DM, Lentzen G, Khayyal MT. Novel effects of ectoine, a bacteria-derived natural tetrahydropyrimidine, in experimental colitis. *Phytomedicine.* 2013;20(7):585–591. doi:10.1016/j.phymed.2013.01.009

International Journal of Nanomedicine

Dovepress

## Publish your work in this journal

The International Journal of Nanomedicine is an international, peer-reviewed journal focusing on the application of nanotechnology in diagnostics, therapeutics, and drug delivery systems throughout the biomedical field. This journal is indexed on PubMed Central, MedLine, CAS, SciSearch<sup>®</sup>, Current Contents<sup>®</sup>/Clinical Medicine, Journal Citation Reports/Science Edition, EMBase, Scopus and the Elsevier Bibliographic databases. The manuscript management system is completely online and includes a very quick and fair peer-review system, which is all easy to use. Visit <http://www.dovepress.com/testimonials.php> to read real quotes from published authors.

Submit your manuscript here: <https://www.dovepress.com/international-journal-of-nanomedicine-journal>